Repeating Earthquakes in the Darfield Region, New Zealand

May 2013

By
Ryan S. Armstrong

Colorado College Department of Geology

Class of 2013

Advisors:

Megan Anderson, Colorado College Department of Geology

Ellen Syracuse, University of Wisconsin-Madison Department of Geosciences

Clifford Thurber, University of Wisconsin-Madison Department of Geosciences

Abstract:

The M 7.1 3 September 2010 Darfield, New Zealand, earthquake ruptured a previously unknown fault system. Fault-slip models (e.g., Beavan et al., 2010; Holden et al., 2011; Eliott et al., 2012) have been calculated using InSAR, GPS, and seismic data. They show that although the rupture initiated on a SW-dipping thrust fault, the majority of fault motion was right-lateral strike slip from the surface to 10 km depth. The InSAR data used in the geodetic model provide the cumulative ground motion due to the Darfield earthquake and some early aftershocks, while the seismic model utilizes waveforms for the mainshock, limiting the solution to slip during the initial rupture.

This study utilizes cross correlation methods to identify repeating earthquakes within continuous seismic waveforms from the Canterbury region, New Zealand between September 2010 and January 2011. Repeating events indicate portions of fault segments that are not locked, possibly due to high pore pressure (Bisrat et al. 2012), and thus can indirectly identify locked areas of fault segments. Despite the fact that our method initially recognized 8 groups of potentially repeating earthquakes, a cross correlation check at a second station indicates that none of the identified earthquakes are truly repeating earthquakes. Our method provides negative results, which indicate repeating earthquakes may not be present within the Darfield fault complex, although it remains unclear whether they are truly absent or the methodology is not sufficient to detect them. While our method failed to identify repeating earthquakes, it possibly identified clusters of events with similar focal mechanisms In theory, our study shows a direct relationship between the compactness of a cluster and the similarity of focal mechanisms.

Table of Contents

Introduction

In tectonically active areas, prediction of earthquake size and timing is both important and difficult, and although scientists haven't found any reliable methods, risk assessment has improved dramatically through more well-resolved plate motions and fault movement over short timeframes of tens to hundreds of years.The improvement of risk assessment allows for more accurate hazard assessment of fault zones as well. New repeating earthquake (RE) studies, such as Yamashita's (2012) study in Japan, are one form of new insight into temporal stress changes within seismically active fault systems. Repeating earthquakes are events that occur with the same location, focal mechanism, and magnitude. Yamashita used REs to analyze interplate coupling, or how smoothly the tectonic plates slide past each other in a subduction zone. By finding how many times earthquakes repeated within a fault segment and the magnitude of these earthquakes, he calculated slip rates of different parts of the subduction zone due to these small events. Thus, he also predicted which zones were more thoroughly locked, exhibiting less slip. Other studies such as Bisrat et al. (2012) and Chen et al. (2010) have studied swarms of repeating earthquakes within both periods of high and low seismicity in order to try to characterize how and why these events might occur.

New Zealand's tectonic setting is unique in that the Australian plate subducts beneath the Pacific plate in the south, and the Pacific plate subducts beneath the Australian plate in the north (figure 1). As a result, there is a zone of right-lateral strike-slip motion, the New Zealand Shear Belt (NZSB), which acts as a transitional zone and contains many separate fault segments including the Alpine Fault. (figure 2). The

Christchurch fault zone (figure 3), responsible for the September 2010 and February 2011 earthquakes, is a primarily EW-trending, right-lateral fault zone, with some segments of oblique slip. This fault zone, previously unknown before the 2010 event, is partially responsible for the release of tectonic stresses within the NZSB between the Pacific and the Australian plate. Although the Christchurch fault zone is about 100 km south of the previously known Alpine Fault (figure 2), its primarily right-lateral slip direction with some small thrust component suggests that it is most closely related to the Alpine fault. Before the 2010 event, scientists believed that the nearly 1000 km long Alpine fault and associated fault strands accommodated all of the strike slip motion required in the tectonic setting.

On 3 September 2010 a M 7.1 earthquake ruptured the western edge of a previously unrecognized fault zone near Christchurch, New Zealand, hereafter referred to as the Christchurch fault zone. On 21 February 2011 a M 6.3 earthquake struck southeast of Christchurch (Elliott et al., 2012). The rupture devastated the Central Business District and claimed 180 lives (NZPA, 2011). While decades of study, such as detailed historic earthquake records, constrain the hazard posed by comparable strike-slip fault zones such as the San Andreas Fault Zone or the North Anatolian Fault, the historic earthquake record of the Christchurch fault zone is unclear paleoseismic studies revealed no previous rupture in the area, which we discuss in the background As a scientific community, we now need to build knowledge of fault dynamics about the Christchurch fault zone through other studies such as repeating earthquake studies to characterize short term fault movement, Coloumb stress studies to examine fault loading, and possibly even active source geophysical studies to image potential below surface fault structures.

After the surprising rupture in the Canterbury region, scientists need to begin reevaluating the seismic hazard in Christchurch not just due to the Alpine fault, but also the Darfield Fault Complex. Multiple studies (e.g., Beavan et al.,2010; Elliott et al., 2010; Holden et al., 2011) calculate fault-slip models of the initial rupture (figure 3), but to date, there is still much work to be done before the fault zone dynamics are well understood, especially in comparison to other fault zones near large cities like the San Andreas fault zone near San Francisco. This study aims to locate repeating earthquakes within the newly identified fault complex by utilizing a cross correlation method on 4 months of continuous seismic data for the aftershock sequence of the 3 September 2010 rupture, which begins about ten days after the earthquake. Our study failed to indicate repeating earthquakes within the Christchurch fault zone, but possibly identified clusters of earthquakes with slightly different focal mechanisms and locations.

Background

In order to understand how repeating earthquakes might occur and what they can tell us about our study area, it is important to understand some basic seismology concepts including fault physics, the seismic cycle, and the earthquake radiation pattern, as well as the geology of the Canterbury Region and the dynamics of the 3 September 2010 mainshock. We will also touch on earthquake locations given that it is a vital step in checking our cross correlation method.

The Physics of Fault Movement and the Seismic Cycle

An understanding of fault dynamics and the seismic cycle can be built up from basic physics combined with simple geological concepts. Tectonic stresses manifest themselves through either brittle or ductile deformation, depending on characteristics such as rock elasticity, crustal temperature, and the time scale of applied stress. Brittle deformation leads to faulting; however, fault behavior varies greatly depending on multiple factors, including the normal stress on the fault plane, which can be affected by pore pressure, the friction or shear coefficients of the materials within the fault, and the shear stresses (Stein and Wysession, 2003).

These are, in the simplest sense, governed by the basic physics equation for friction:

$$F_F = \mu F_N \quad (1)$$

where F_F is the force due to friction, which is parallel to the fault plane and opposing the force which causes slip, μ is the coefficient of friction, with higher values of μ corresponding to higher frictional forces, and F_N is the normal force, or the force between

the two surfaces in question, acting normally to the two surfaces. In a simple example of a box sliding along a surface, both the weight of the box, or the normal force, and the interaction between the bottom of the box and the floor, or the frictional coefficient will affect how much frictional force is created. The frictional force becomes the base of our understanding, because until the force trying to move the box overcomes the frictional force, the box won't move, just as a fault won't move until the tectonic stresses overcome the frictional forces holding the fault in place. Seismologists usually consider stresses as opposed to forces because stresses take into account the area upon which the force is acting and is thus more applicable to rocks within the earth and such structures as fault planes. Since we know that stress is simply force applied over an area, if we are dealing with a uniform infinitesimal area, we can modify our friction equation to:

$$\sigma_{cf} = \mu\sigma_n \quad (2)$$

where σ_{cf} is the critical failure stress or the level of stress when the fault will begin to move, σ_n is the normal stress, and μ remains the same (Stein and Wysession, 2003).

In geology, we typically refer to stress directions as σ_1, σ_2, and σ_3, which are a set of basis vectors that as a sum represent the total stress at one point. They are numbered σ_1 to σ_3 as the strongest to weakest stresses respectively (figure 4; Stein and Wysession, 2003). Because the normal stress on a fault plane is defined as the stress vector perpendicular to the fault plane and the force of friction, which holds the fault in place, is defined as being parallel to the fault plane, we would need to calculate a new set of vectors from our σ_1, σ_2, and σ_3, for each fault plane in order to find vectors with the correct orientations to be the normal stress and failure stress vectors. Without explicitly doing this calculation, it is evident that fault planes perpendicular to σ_1 will exhibit the

highest normal stresses, while those containing σ_1 will tend to exhibit lower normal stresses, which are determined by σ_2 or σ_3 (figure 4).

While normal stress is a primary contributing factor to fault strength, the presence of fluids can raise the pore pressures within the faulting rock, which can affect fault strength as well. At any given point within the subsurface, pore pressure exerts equal stresses outward in all directions. As a result, on a fault plane, the pore pressure acts in the opposite direction of the normal stress, which lowers the effective normal stress on the fault plane,

$$\bar{\sigma} = \sigma - P_f \quad (3)$$

where $\bar{\sigma}$ is the effective normal stress, σ is the normal stress, and P_f is the pore pressure (Stein and Wysession, 2003). Substituting the effective normal stress (equation 3) for the normal stress in equation 2 leaves us with a new friction formula,

$$\sigma_{cf} = \mu(\sigma - P_f) \quad (4)$$

As a result, we can expect that less tectonic stress will be required to rupture a fault as the pore pressure increases, since both the pore pressure and the normal stress will always be positive within the earth. As we will see, the normal stress is not the only variable affected by increased pore pressure.

Aside from the effective normal stress, the largest contributing factor to the frictional stress is the coefficient of friction μ, which we will be called the shear modulus in our fault discussion. It is important to note that the shear modulus and the coefficient of friction are closely related in that a higher shear modulus value is associated with more required stress to achieve the same amount of strain, while a higher coefficient of friction value is associated with more required stress to cause fault movement; the shear modulus

deals with ductile deformation while the coefficient of friction deals with brittle deformation. In reality, while we use the coefficient of friction to talk about sliding dynamics in physics, fault zones tend to contain ground-up material within the fault plane (gouge) which behaves ductiley, and so the shear modulus becomes a more applicable variable. Thus, the shear modulus (also denoted by μ) will vary by rock type, rock competency, and presence of fluids. Shear strength directly relates to the connection of molecules or grains, whether through chemical bonds or grain cementation; therefore, strongly cemented sedimentary rocks will have high shear strength, but not as high as crystalline rocks, which are more thoroughly locked together. For this reason, unconsolidated material such as alluvium has extremely low shear moduli in comparison to those of cemented sedimentary rocks, which are lower still compared to volcanic or metamorphic rocks. In the Canterbury Region, for example, we would expect the Pleistocene alluvium to rupture more easily than the underlying Triassic sandstones because of the sandstone's coherency and thus a higher shear modulus(Elliott et al., 2012); also their common existence at depth and density due to burial will increase the shear modulus as well (Lillie, 1999). Additionally, we would expect the presence of fluids to reduce the shear modulus values of most rocks because of its ability to reduce coherency and act as a lubricant between grains.

The Seismic Cycle and Aftershocks

By expanding on the previous box example we used to explore fault friction, we can imagine a system in which a box is being pulled across a surface by a rubber band. A constant pull on the rubber band, analogous to tectonic forces, causes the force on the box to increase proportionally to the spring constant, k, of the rubber band:

$$F = -kx \quad (5),$$

where x is the displacement of the rubber band from its unstretched position. Eventually, the force the rubber band exerts on the box will grow large enough that it will pass the critical force, which is the amount of force required to overcome the frictional force as we defined it in equation 1. Because the friction coefficient for a dynamic object is always lower than the friction coefficient for the same object at rest, the box will continue to slide until the dynamic force of friction is larger than the spring force from the rubber band. As a result, even though the rubber band is being pulled at a constant rate, the box will move in a stick-slip motion because the friction coefficient will be changing (Stein and Wysession, 2003).

The rubber band and box model offers a nice analog for the perfect fault conditions, when there is a perfectly planar fault with unchanging friction coefficients and stresses that ruptures in its entirety every time. Unfortunately, most faults cut through varying rock types, which changes the shear modulus of the fault spatially, and different parts of the fault tend to rupture at different times. This causes stress changes regionally after a partial rupture, referred to as Coulomb Stress changes. Most importantly, faults are often complex, including branches or orientation changes (Stein and Wysession, 2003).

Due to these complexities, large earthquakes are often followed by a series of earthquakes referred to as aftershocks. Aftershock ruptures tend to exhibit a similar slip direction to the initial earthquake due to consistent tectonic stresses in the region. They also tend to be at least 1 order of magnitude less energetic than the initial event (Stein and Wysession, 2003). Seismologists consider the aftershock sequence of the M 7.1 September 4, 2010 earthquake to be an exceptionally long and unique aftershock

sequence due to the unusually large M 6.3 aftershock on February 21, 2011 and the extensive time period during which aftershocks have continued (GNS Science, 2/25/2011). However, when discussing the relationship between the movements during the two events, it is important to note that there was no overlap in slip location between the 2010 and 2011 events (figure 3). Since the rupture areas did not overlap, the initial rupture may have further increased an already nonzero stress field near the 21 February 2011 fault segment, therefore, causing a larger stress drop for this event than the other aftershocks. However, GNS scientists still label the February event as an aftershock of the September event because the rate of aftershock frequency quickly decayed back to the decay rate before the February event (GNS Science, 2/25/2011).

Geology and Tectonics of the Canterbury Region

The tectonic complexities of New Zealand lead to a zone of high deformation in the mountains on the northwestern side of the South Island where faulting is relatively common (the NZSB, figure 2). An area of relatively lower deformation exists to the south of the mountains where alluvium settles to form the Canterbury Plains (Lillie, 1980). The NZSB is composed of the Alpine Fault and many of its northern splays in the Marlborough Fault Zone, such as the Hope Fault, which trend toward the North Island (figure 2). The stresses that cause compressive tectonics arise from subduction along the plate boundary to the northeast and southwest of the NZSB, and are also responsible for the right-lateral motion of the NZSB. The plate boundary in New Zealand has developed a bend as the plates on either side of the NZSB subduct in opposite directions, thus causing the trenches to migrate away from each other. As a result, the NZSB is oriented at an oblique angle relative to the plate movement, which allows for a component of

transform movement as well as a component of compression within the shear belt. The Canterbury Plains, which lie between the Banks Peninsula and the Southern Alps (figure 2), have been relatively geologically inactive by comparison, evident by the general lack of uplift and high rates of alluvial deposition. The geology of Kaikoura to the north of the Canterbury Plains (figure 2) contains exposures of Triassic and Jurassic Torlesse basement rock, which is the greywacke that also makes up much of the Southern Alps (Lillie, 1980). Because the Canterbury Plains are relatively less deformed than areas such as Kaikoura, which is closer to the plate boundary, the same layers that are exposed in Kaikoura are generally found to be flat lying and covered by gravelly alluvium in the Canterbury Region. The alluvial cover, which is being actively deposited, coming out of the Southern Alps in large alluvial fans, dates from the Pliocene to the Pleistocene, indicating that this time period relates to the start of uplift of the Southern Alps, which is still continuing today (Elliott et al., 2012).

Historically, the segments of the Alpine Fault and Marlborough Fault Zone have been the most significant to the Canterbury Region with respect to earthquake hazard, with the Hope Fault last rupturing in a M 7-7.3 earthquake in 1888 (Quigley et al., 2010). However, on 3 September 2010, a previously unknown fault ruptured, producing a M 7.1 earthquake to the south of the known Alpine Fault complex (figure 2).

The 3 September 2010 Slip Model

Fault-slip models for the M 7.1 3 September 2010 earthquake (e.g., Beavan et al., 2010; Holden et al., 2011; Eliott et al., 2012) utilize interferometric synthetic aperture radar (InSAR), Global Positioning System (GPS), and seismic data (figures 3 and 5) to produces slip amounts and errors on specific fault segments. They show that although the

rupture initiated on a SW-dipping thrust fault, segment 7 (figure 3), the majority of fault motion was right-lateral to right-oblique strike slip (segments 1-5) from the surface to 10 km depth. Elliot et al. (2012) were the first to include in their model a NS-trending left lateral transform fault (segment 6 in figures 3 and 5). Although this fault segment didn't show surface rupture, it clearly appears to be due to the relatively high level of seismicity in the area (figure 4). The varying orientation of the fault segments within the fault complex cause different motions on different fault segments (e.g., right-lateral, left-lateral, or thrust) as we will discuss below, but the dominant motion was right-lateral (figure 2).

The new surface ruptures are EW-oriented with up to 4 meters of right lateral displacement in some areas as well as up to 1 meter of vertical displacement at bends in the rupture (Quigley et al., 2010). The new fault segment extends eastward toward the city of Christchurch (fault segments 2, 3, and 4 in figure 3). Because the new fault complex is entirely within the Canterbury plains, it ruptured only river alluvium at the surface, which had been deposited by the end of the last glaciation about 16,000 years ago. This would typically suggest that the fault had not ruptured in 16,000 years or historical surface deformation would have been present, but in reality, establishing a detailed historical earthquake record for the region is difficult for multiple reasons, including the possibility of events not causing surface rupture that persists over time or the cultivation of the Canterbury Plains for agriculture, which would masking geomorphological evidence for past ruptures. The physical characteristics of the sediment could be responsible for both of these two possibilities. Because young, gravelly alluvium comprise the Canterbury Plains, and evident surface rupture requires a distinct offset of

materials, the high mobility of the sediment causes it to effectively mimic ductile deformation and makes it difficult to identify distinct ruptures geomorphologically. Additionally sediment may be physically transported to erase any potential evidence even if it initially deformed brittley instead of ductiley. Therefore well-cemented layers deeper in the earth may rupture without the surface above ever exhibiting rupture. A good example of this is the NS-trending fault (segment 6 in figures 3 and 5). Though fault models supply strong evidence that the fault ruptured during the main shock and aftershocks were recorded along its length, no surface rupture was recorded.

In order to understand the complexities of the newly discovered fault segments' movements it is necessary to relate the deformation to the tectonic stresses and the resulting regional strain. Because the tectonic situation of New Zealand is so complex, it is difficult to attribute regional stress directions to a single type of plate movement (either compressive or transform). Since we actually have a transition between these two types of motion, we can deduce that along the Alpine Fault there is a certain amount of compressive stress as well as shear stress, which in theory would lead to both thrust faulting and transform faulting or the combination, oblique or transpressive faulting. As this logic suggests, this combination of stresses results in the deformation represented by the focal mechanisms given by Elliott's (2012) slip model (figure 3). In his model, we see many E-trending strike slip focal mechanisms and a few NE-trending thrust fault focal mechanisms.

Conveniently, Wallace et al. (2007) implemented an elastic rotating block model to assess strain rates for all of the Southern Island of New Zealand, including the Canterbury Region. By using velocities at different spots on the plate derived from GPS

data, they were able to come up with an internal principal contraction direction of 110-120° east of north within the Canterbury Region (figure 3). If we think about the orientation of fault segments in Elliot's (2012) slip model we can attribute to them types of faulting which would result in a similar contraction direction. Fault segments such as segments 7, 8, and 9 (figure 3), which are nearly perpendicular to the overall contraction direction exhibit thrust movement, while fault segments such as segments 1-6 and 10, which are more parallel to the contraction direction exhibit transform. The total contraction direction even fits the slightly oblique slip that Beavan calculated in his 2010 slip model [figure 6; (Beavan et al., 2010)].

Wave Radiation, Earthquake Location and Tomography

When a fault ruptures, seismic waves propagate outward from the point source. Depending on the orientation of the fault plane and the direction of slip, different types of waves will propagate with different strengths in different directions and with different polarities (up or down movement). Fault ruptures create two types waves, called body waves: compressional or primary waves (P), which cause movement parallel to the direction of propagation (like sound waves), and shear or secondary waves (S), which cause movement perpendicular to the direction of propagation. These two types of waves travel at different speeds, and are instrumental in earthquake location and repeating earthquake studies as a result.

Locating earthquakes can be a very uncertain process, but if locations are reliable, we can use them to identify repeating earthquakes, which we have yet to describe in detail. In order to accurately locate an earthquake epicenter (latitude, longitude, and origin time) we need accurate first arrival times for the primary (P) and secondary (S)

waves as well as an accurate velocity model. First arrival times are the time when a P or S-wave first causes earth motion beyond the typical background noise of the region. Therefore, this time is representative of the earliest wave front arriving at the seismic station. By calculating travel times to seismic stations from large earthquakes with well-known locations, seismologists develop velocity models, which describe how seismic velocities change with depth. Because models exist for both P-waves and S-waves in most regions of the Earth, we can write an equation to calculate the distance from a given station to the epicenter from the epicenter of an earthquake with an unknown location:

$$T_s - T_p = X(1/V_s - 1/V_p) \quad (6)$$

where $T_s - T_p$ is the differential time between the arrival of the two types of waves at a station and $1/V_s - 1/V_p$ is the inverse of the known velocity differential of the two waves within the raypath (see raypath definition in figure 8). Therefore X is the distance to the epicenter from the seismometer. By drawing a circle (or spheres for a hypocenter) with radius X around the seismic station, we triangulate the earthquake epicenter by repeating this process with at least 3 stations (figure 9).

The previous equation assumes a completely homogenous velocity model, which we know is not true even on a global scale. one-dimensional velocity models assume laterally constant velocities, which is acceptable on a global scale because we primarily see the largest changes at large boundaries such as the Moho. Similarly, because of the principle of original horizontality, one-dimensional velocity models function well for areas of little geologic deformation. Once deformation begins to cause lateral changes in rock type, there will also be a lateral change in velocities. The best way to account for laterally varying velocities within the crust is through tomographic studies. By using

multiple events with different raypaths, velocities are calculated by using matrix algebra. Put simply, a tomographic study split the earth up into 3-d cells, and varies the velocity of each cell in order to minimize the error in the predicted arrival time in comparison to the known arrival time. The key to this process is utilizing arrival times from enough raypaths that part of multiple raypaths pass through each cell in order to constrain the velocity of that cell. The end result is a final velocity model that varies in three dimensions, and predicts a percent change in velocity from the initial assumed velocity model in each cell.

P-wave and S-wave Radiation

Because of the nature of each of these waves, S-waves and P-waves will show different amplitudes at different directions of propagation relative to the fault plan S-waves created propagating 90° to the fault plane will be at their highest amplitude, while P-waves at the same angle will have very weak amplitudes. Additionally, 45° to the fault plane the P-waves will be at their highest amplitudes, while the corresponding S-waves will have very weak amplitudes. At other propagation directions the relative strength of the two wave types will tend to be more similar. Figure 7 shows the radiation patterns for P-waves and S-waves with respect to a fault plane.

Repeating Earthquakes

Just within the past 20 years, seismologists started searching for repeating earthquakes (REs), which are earthquakes with the same location, focal mechanism, and magnitude. Repeating earthquakes tell us that certain fault patches are consistently rupturing the amount under consistent stress conditions. Studies such as Chen (2007)

have even empirically linked the recurrence interval of repeating events to their magnitude. We can more accurately identify locked areas of the fault segment and more quantify stress build-up by analyzing which fault patches slip and how much they slip over time. RE analysis relies entirely upon similarity of the seismic waveforms. In theory, a seismic waveform is a combination of the sense and magnitude of movement from the source rupture (termed a slip function); the effect of the geology, such as reflections and refractions that change the phases received at the station or velocity differences between P-wave and S-waves (termed the Green's function); and how the seismometer responds to an incoming wave (or instrument response). These three functions combine through a mathematical process, convolution, which produces the final seismogram (figure 10). More complex slip functions and Green's functions lead to longer and more complex seismograms. Because we have established that these three functions are the only contributors to seismogram shape, we can say that very similar waveforms are a direct result of similar slip functions, Green's functions, and instrument response. Moreover, if the same seismic station (thus the same instrument response) records the two seismograms, a similar Green's function implies a similar raypath and location for the earthquakes. REs tend to be small amplitude events due to the fact that a smaller rupture will tend to have less complexity spatially and temporally represented by a simple pulse instead of a complex slip function that we would expect from a large rupture. Therefore, the smaller events lend themselves to being more easily repeated due to the simplicity of the event. Figure 11 illustrates a swarm of repeating earthquakes from the New Madrid Fault Zone. Note the similarity in the peaks of the waveform just after 1.0 s and 2.0 s;

these are the first P-wave and S-wave arrivals and correlate very strongly between all of the events within the swarm.

Methods

Our repeating earthquake study relies on cross correlation methods, specifically two codes, *corr_scan* and *clone_fixed* (MacCarthy and Rowe, 2005) to identify the potential repeating earthquakes. This method compares an initial waveform (the master trace; figure 12) to a longer section of seismic data from the same station by stepping the shorter waveform along the continuous dataset and assigning a correlation coefficient based on the similarity of the traces at each time step. As a result, times in the continuous dataset with very high correlation coefficients indicate a possible repeated earthquake. Our seismic network consists of 13 broadband seismometers deployed by the University of Wisconsin-Madison and the Victoria University of Wellington (figure 13) directly after the 3 September 2010 rupture. This dense network provides a fantastic set of continuous data in which to search for repeating earthquakes. In order to successfully execute this method, we parse the continuous seismic data from each station into hourly segments and organize it into folders labeled by the day of the year and hour so that the computer's memory can more easily handle the files. We also create control files, which tell the two codes where the master trace is located and where the continuous data for each seismometer is located. For the initial cross correlation, I set up control files for stations DAR3, DAR6, DAR7, and DAR8 due to their general proximity to the main fault segments.

Using the fault segment coordinates from Elliot et al. (2012) and the entire earthquake catalog of the Canterbury Region (GeoNet, 2013), we create separate earthquake catalogs for each fault segment so that we can begin to choose master traces one fault segment at a time in order to keep track of which earthquakes have been cross

correlated. Higher frequency waveforms tend to produce more reliable results, because they introduce more overall amplitude variance within the waveform and therefore the cross correlation program can more easily differentiate matching waveforms from low-frequency noise. Because of this, I sort through the fault segment catalogs and chose high frequency p-wave arrivals with strong and clear P-wave arrivals as the master event traces, from one of the 4 stations mentioned above. Next, I use SAC (Seismic Analysis Code) to cut the trace to isolate the segment of the waveform that starts 0.3 seconds before the arrival and end 0.4 seconds after the arrival, a total of 0.7 seconds (figure 12). We chose such a short time window to keep the computations quick; we will discuss the consequences of this choice later.

Clone_fixed passes the aforementioned waveform step by step at 0.1-second steps across the seismic station from which it was cut. The program attributes to each step a correlation value from 0 to 1, which represents the amount of similarity between the master trace and the 0.7-second section of continuous data at that point. Finally, *corr_scan* reads the output file of *clone_fixed*, which describes the correlation values of each time step. The program moves all waveform segments with correlation values labeled over a specified threshold (e.g. 0.80, 0.85, or 0.90) into the destination folder. We used a cross correlation coefficient of 0.90 because it most consistently produces the greatest number of potential repeating events. Lower coefficients produce large numbers of what the computer thinks are repeating events, but a human check reveals that many are clearly not repeating events. A 0.95 cross correlation coefficient rarely selects events besides the master trace itself, which should in theory have a correlation of 1. After this process, the destination folder contains similar events according to the computer codes.

Unfortunately, the cross correlation codes are imperfect and their output waveforms require review. Because our master trace did not have a P arrival until 0.3 seconds into the seismic trace, any waveform that shows significant movement in the first 0.3 seconds is immediately removed from the potential repeating events folder. The Matlab program GISMO (West, 2007) organizes the remaining waveforms into hierarchical clusters by their correlation coefficients. The resultant diagram is a tree-like structure, which clusters the waveforms with the highest similarity by more closely link in them in the hierarchical diagram (figure 14).

In order to check that our process works successfully to find repeating earthquakes, we employ two additional systems of secondary checks, the first of which is the earthquake locations. Because potential REs, due to their small magnitudes, are often not yet cataloged in the list of known earthquakes already located (GeoNet, 2013), we must locate them by picking P-wave and S-wave arrivals at many stations and then transferring that data into the earthquake location software TomoDD (Waldhauser and Ellsworth, 2000; Zhang et al., 2003). TomoDD uses multiple iterations of tomographic calculations to tweak the input velocity model and event locations in order to reduce travel-time residuals. Our initial velocity model is a one-dimensional average of the Darfield Region from the 3-dimensional model of Eberhart-Phillips et al. (2010). After all iterations are complete, we are left with a final velocity model as well as earthquake locations, which are now all located relative to each other. Ideally, the end result should provide groups of earthquakes with similar waveforms that originate from the same place on the fault segment.

Because earthquake location errors can be difficult to constrain (Anderson and Myers, 2010) we also employed a final check for each potentially repeating group by cross correlating the same master event arrival at a second station (DAR3) with the DAR3 continuous data. Since REs should in theory produce similar seismograms at any given station for all events, the cross correlation at the new station should yield all of the waveforms associated with the events of the RE group being tested. If this process produces either no repeating events or different repeating events than the first cross correlation, then the group of earthquakes is not an RE group.

Results

First Cross Correlation

The combination of the cross correlation codes at a coefficient threshold of 0.9 within both *clone_fixed* and GISMO produced 9 groups (0-8; all groups shown in appendix) of potentially repeating earthquakes out of about 120 tested master traces at either station DAR6, DAR7, or DAR8. Repeating earthquake group sizes ranged from 16 events (group 4; figure 14) to 66 events (group 3; figure 15) with master traces originating from various fault segments. We found three of these groups using master traces from segment G (figure 13), two each from segments A and C, and one each from segments D and E. Segments B and F didn't yield any potential repeating earthquakes over this time period by our method.

Earthquake Locations

The consistency of earthquake locations for the groups is highly variable between groups of events, such as group 4 being clustered (figure 16) (latitude, longitude, and depth) and group 6 being very poorly clustered (figure 17). Our location errors were given by the program as time residuals (the predicted time of arrival minus the true time of arrival), and vary from about -200 to 200 milliseconds, which, given a velocity model between 5 and 10 km/s would imply spatial location errors of about 1 to 2 km. I will elaborate on the reliability of these errors in the discussion. The events within each group varied temporally as well with events occurring in September, October, November, and December for all groups.

Second Cross Correlation

Station DAR3 recorded each of the events associated with the master traces of our 9 potential repeating earthquake groups. We use the record of these events at DAR3 as the master trace for our second cross correlation. As we established earlier, the cross correlation of these new waveforms across the DAR3 continuous data should produce the same repeating events as the first cross correlation test. The cross correlation program labels the potential repeating events by the date and time that the trace starts. Unfortunately, when we ran our second cross correlations, we get potential repeating events, but none of them have time and dates remotely similar (most events not even within one calendar day) to those identified by the first cross correlation at the other DAR station. This tells us that the events we had initially identified as potential repeating events are not producing the same seismic shape of signal for each event across all stations, and are by definition not repeating events.

Discussion

Our results raise many important questions, especially regarding their importance and validity. There are many different ways to interpret our data. Our method may be insufficient to identify repeating earthquakes or this fault zone may not have produced repeating earthquakes at this time. To pinpoint what the most likely reason for our results is, we will consider our results in light of our and others' cross correlation methodology, consider some potential issues with earthquake location accuracy, and finally discuss how these repeating earthquakes might relate to the seismic cycle.

Cross Correlation Method

The cross correlation method required us to choose arbitrary correlation coefficients so that our method would provide us with potential repeaters. All of our potential repeating events were correlated to a 0.90 coefficient with our window length of 0.7 s. This coefficient value is within the range of values used in other studies (e.g., Hansen et al., 2006; Bisrat et al., 2012), which tend to range from 0.55 to .95 depending on window length and background noise levels. Cross correlation studies can also vary by window length and the window step size, which were 0.7 seconds and 0.1 seconds, respectively, in our study. Two key cross correlation studies with drastically different cross correlation methods in order to aid the understanding of parameter variations, such as time window length and correlation coefficient thresholds, within the cross correlation methods.

Hansen et al. (2006) attempt to use the cross correlation method to identify cross correlate similarly shaped P-wave arrivals from a set of already well-located earthquakes, with a goal of increasing earthquake location accuracy. Because the earthquake catalog

was already well-defined, the cross correlation was not over the continuous data set, but only between already located earthquakes, which were within a 10 km distance of each other. Therefore, this method has an earthquake location constraint built into it prior to cross correlation and any similar earthquakes determined by this method should have highly similar travel times at each station. Once the computer finds similar clusters within these closely grouped earthquakes, the program automatically adjusts the P-wave arrival picks to make sure that the picks are made at a consistent point within the similar waveform. Rowe et al. (2006) showed this method to reduce human error in picking arrivals. Hansen utilizes a relatively short time window of 1.00 s in order to focus on the arrival of the P-wave and exclude the S-wave arrival. Though Hansen doesn't specify the value of the window step size, we can assume that it is likely low due to the short length of the window itself. Similar to our method, Hansen also uses a relatively high correlation coefficient threshold of 0.90 for cross correlations on the stations with the highest signal to noise ratios and lower coefficient thresholds (0.80) at other stations which exhibited lower signal to noise ratios, in order to account for the random variability in noise.

Bisrat et al. (2012) employ very different parameters in their cross correlation study, because they aimed to identify true repeating earthquakes as opposed to similar P-wave arrivals. Bisrat tests window sizes of 1.00, 1.28, 2.56, and 5.12 s and step sizes of 0.10, 0.15, and 0.20 s and finds that windows of 5.12 s and steps of 0.20 s produce the highest correlation coefficients for the data set. Because of the longer window, the similar waveforms identified contained multiple wave phases such as direct S-waves arrivals in addition to the P-wave arrivals. Bisrat uses significantly lower coefficient thresholds ranging from 0.55 for stations with low signal to noise ratios to 0.75 for stations with

high signal to noise ratios because the longer time windows in increase the total amount of variability between the waveforms and thus lower the overall similarity coefficients.

These two studies use drastically different window lengths because of the purpose of the respective studies. Bisrat et al. (2012) provides an insightful explanation of this issue:

> "A very small window length (compared to the wavelength of a phase) may give high CC values that do not reflect similarity of the full waveform of the phase. In contrast, a longer window may yield CC values strongly affected by signals different from the phase of interest."

Therefore, the aims of the two studies fit well into their chosen windows. Hansen et al. (2006) didn't include the arrival of the S-wave at all in the time window, because they simply wanted to match the timing of the P-wave arrivals in order to improve location techniques and focal mechanism accuracy. Bisrat et al. (2012), on the other hand, cared about the both the time differentials of the arriving phases as well as their first motions, so the window length reasonably contained the arrival of multiple phases. As a result of Bisrat's statement, we can also conclude that the differing correlation coefficient thresholds should be a result of the differing time windows. Since the longer time windows will show more variation outside of phase over time (including noise), the overall correlation coefficient will tend to be smaller.

In light of these two studies, it seems that while our correlation coefficient threshold was appropriate for indicating similar P-wave arrivals, our short window length may not have been appropriate for identifying completely repeating events. Without including the S-wave arrival within the master event time window, we are unable to

correlate the differential times of phases between our potential repeating events; therefore it could be difficult or impossible to identify events that are coming from exactly the same location. Even using a separate cross correlation of S-wave arrivals to confirm potential repeaters would not be sufficient, because it is possible that the potential repeaters by our smaller window at such a relatively high coefficient may not find the same events as a longer window would, given its lack of multiple phases within the window.

In an attempt to sidestep the issue of earthquake location errors, which we will discuss next, we chose to cross correlate the corresponding earthquake arrival from each master trace event at a different station. Because of the path difference from a specific event location to different stations, the two different stations will exhibit different seismic signals for the same event because of the relative locations to the focal mechanism as well as differences in structure. However, when the waveform of the first arrival at the second station is cross correlated with the continuous data of the second station, repeating earthquakes should still be represented by high correlations. Therefore, running cross correlations at a second station for each group should produce the same repeating events as the first station did for that same group. The most promising example was group 4, which had initially represented our most likely repeating group from our first station, DAR6. The cross correlation of the same event at a second station, DAR3, yields potential repeating events, however none of the events overlap with the repeating events indicated by the cross correlation at station DAR6 even while using varying correlation coefficient thresholds to account for potential noise differences. This result strongly indicates that our potential repeating events are in fact not true repeating events in both

time and space. However, due to the fact that our study only cross correlated a small percentage of all of the aftershocks that have occurred over the 4-month study period, it is still possible that repeating earthquakes are present and we did not detect them. A code that could streamline all identified earthquake arrivals into the cross correlation code, rather than certain "picked" master traces from a catalog, in addition to an even more complete earthquake catalog would be necessary to eliminate this problem due to the vast number of aftershocks, some still uncatalogued, within the fault complex.

Earthquake Location Accuracy

Earthquake location accuracy is a difficult topic to address because of the challenge of assigning true errors to earthquake locations. There are many different potential sources of earthquake location error. But two of the predominant sources of error are human error in picking wave arrivals to inaccuracies in the velocity model used in the location, as shown by Anderson and Meyers's (2010) study.

Anderson and Meyers (2010) located 74 Nevada Test Site explosions for which the exact locations are already known, utilizing seismic records from stations throughout the western U.S. Because the locations are already known, they were able to test the reliability of location error with respect to several factors. The study tried to establish a relationship between true location error and the size of the azimuthal gap (the largest radial gap in degrees between two stations that surround an event) for a location (figure 18). They also compare estimated travel-time residuals calculated by a multiple event location program to the actual travel-residuals computed based on the known event locations. Because P-wave and S-wave arrivals are not clear at every station in the

network seismic network, some earthquake locations may not have as many picks as others. Therefore both of these issues are pertinent to our discussion of location accuracy.

However, the azimuthal gap may not even be an issue within our seismic network. According to Anderson and Meyers's (2010) study, large azimuthal gaps are not associated with large and systematic mislocation errors when utilizing a multiple-event location method (figure 19). In our case, even though we have relatively low signal to noise ratios at many of the far away stations, such as OXZ or CCH1 (figure 13), because of our chosen method (tomoDD is a multiple-event location method), it seems that azimuthal gap is likely not a large contributing factor to any possible earthquake location error.

The most intriguing result of Anderson and Meyers (2010) is the discrepancy between reported residuals from the multiple-event location software and the known errors. They tested four velocity models of varying accuracy and in all four cases the reported residuals were significantly lower than the true residuals from the known location (figure 20). Most interestingly, the lowest reported residual belongs to a global velocity model (IASP91), which in theory should be much less accurate for regional locations than the tested regional models. In fact, the global model exhibits the least accurate locations and the highest residuals based on the actual location, but the location code gives very low residuals (figure 20), which Anderson and Meyers attribute to errors in the velocity model being mapped into event mislocation.

Given these results, the earthquake locations calculated from our location residuals should definitely be called into question. Because our initial one-dimensional velocity model used to calculate these locations is a one-dimensional average of part of a

larger velocity model (Eberhart-Phillips et al., 2010), it may lack some detail that has been achieved in more thoroughly studied areas and, therefore, could be prone to large errors. However, because we assume that the geology of the Canterbury Plains is relatively laterally homogeneous in comparison to other regions, the one-dimensional velocity model may be an acceptable fit. Additionally, tomoDD is designed to change the velocity model slightly during each iteration to more accurately reflect the regional model in the final results. Because our study did not explicitly explore the final velocity model in order to check it's reliability, hopefully tomoDD should have improved upon our initial velocity model. After consideration, it seems that our final velocity model may be be well-defined well defined. Therefore, the only other main sources of error left to discuss may stem from minimal station coverage due to a lack of picks or possibly error in picking, which given our velocity model and an assumed average picking error of about 0.1 seconds with velocities varying between 5 and 10 km/s, we have error of between 0.5 and 1 km. Adding to the error calculated from our location residuals, which we now hope may be somewhat reliable, we have a total location error of around 1.5 to 3 km. If we compare this error to our best group, group 4 (figure 16) we can see that this magnitude of error cannot account for the scatter of our potential repeating events. Therefore, if we believe we can trust our earthquake locations, then these events cannot be coming from the same location.

Repeating Earthquakes within the Seismic Cycle

Many repeating earthquake studies have taken place during the interseismic portion of the earthquake cycle [eg., Bisrat et al., (2012); Nadeau et al., (1995); Yamashita et al., (2012)]. However, there have been few studies before ours that have

focused on the postseismic portion of the cycle such as Chen et al. (2010). Chen studied the recurrence intervals of multiple groups of known repeating events in the Parkfield, California region before and after the Parkfield M6.0 2004 event. Interestingly, five of the larger magnitude repeating groups have not recurred after the 2004 Parkfield event, which suggests that something changed to eliminate the small predictable slip on those patches. The patches now either slip aseismically, or have become more thoroughly locked and will not rupture as freely. However, many of the repeating earthquake patches were still active after the 2004 mainshock. Twenty-two of the 34 repeating earthquakes groups not only continued, but increased in frequency. Therefore after a large event, when the segments that don't produce repeating earthquakes continue to move, the increasing stress on most of the repeating patches will cause an increase in the frequency of repeating earthquakes. Conversely, Chen's study also provides evidence of repeating earthquakes being shut off in the form of 5 repeating earthquake groups that hadn't recurred between the 2004 event and the end of the study. This is interesting to us because it shows us that while repeating earthquakes often occur during the interseismic, seismic, and postseismic cycles, albeit at different recurrence frequencies, there is clear evidence for them completely disappearing in between different parts of the seismic cycle. Since Chen et al. (2010) were only searching for previously identified repeating earthquakes families, there is obviously no evidence for the activation of repeating earthquake patches. Because the rate of repeating earthquakes tends to be steady during the interseismic period and other seismicity tends to be low, it may become more apparent if repeating earthquakes are now present in the Darfield Region as the aftershock sequence continues to dwindle.

Possible Explanations for a Lack of Repeating Earthquakes

While it is definitely possible that our region has repeating earthquakes, and we simply missed them because of the limitations of our method, it is important to acknowledge possibilities for why the seismometers might not be picking up repeating waveforms at all. If we go back to our physical understanding of what makes up a seismogram (source function, structural effects, and instrument response), we can divide the possibilities of why the repeating seismograms are non-existent into three realms. Because we know that instrument response will always be the same for one station, only the source function or structural effects could be varying from seismogram to seismogram. The source function can vary simply by the orientation of the focal mechanism with respect to the station or can vary by the amount of slip or slip velocity. So our three possibilities for theoretically not being able to find repeating earthquakes are that the slip function changes, the Green's functions change temporally, or the orientations of the focal mechanisms change slightly.

Differing Slip Functions

The first of the three possibilities is that we don't have a repeating slip in the sense of magnitude or slip velocity but they do occur in the same place on the fault. This would have to mean that the same patch of the fault is not repeatedly slipping in the same way, but as we discussed earlier. Past studies have inferred repeating earthquakes as "unlocked" patches of the fault, which slip more predictably than locked segments when introduced to a certain stress level. In the light of these interpretations, a lack of repeating source functions would imply that this region doesn't have certain sections of the fault that tend to slip in this more predictable manner. Although this may seem unlikely when

these slip patches are present in so many other fault zones, it is important to remember that prior to the 2010 Canterbury earthquake, there was no recorded seismicity within our zone of study. Unless small magnitude earthquakes were merely overlooked due to high noise levels and the lack of a dense seismic network before the mainshock, we know that all segments of the fault were completely locked in order to build-up enough stress to cause a significant energy release in the form of the M 7.1 event.

Temporally Changing Green's Functions

The second possibility for a lack of repeating seismograms is that the Green's function (structure-related part of the seismogram) could be changing temporally, which may affect our methodology more strongly than other methods with longer time windows. Long and Wen (2012) highlight the potential for assessing material change temporally through the use of repeated sources. They extract the difference of the Green's functions from two seismograms with a known repeating source. Because the source signal and instrument response are unchanged temporally between the two seismograms, any difference between the two can be attributed to a changing Green's function. As we discussed earlier, Green's functions can be affected by varying stress fields or small cracks, which may change the bulk or shear moduli on a small scale. Larger earthquakes can change moduli on a large-scale, by causing large structural changes, which cause reflections and refractions and different phases as a result. These small-scale changes may change the greens function, but not significantly enough to create new reflections or phase arrivals. Large ruptures, which create significant movement of geologic boundaries and may open larger cracks within the fault structure would affect both the wave velocity, but more importantly reflections within the raypaths. Therefore, we would expect that

because of our geologically short time scale and small ruptures, any changes in our Green's function would be caused by minimal fault movement from aftershocks, which would not be associated with movement capable of causing large scale geologic deformation. Instead, we would need to attribute Green's function changes to temporal stress changes over time caused by the complex movement of the fault segments over the duration of the aftershock sequence. Because our selected time window doesn't include any phase arrivals besides the P-wave, our cross correlation methodology could be more prone to small changes in the Green's function than methodologies that utilize a longer cross correlation window such as Bisrat et al. (2012). These studies may not be affected by such small changes due to the high correlation between larger amplitude phase arrivals such as the P and S-wave first arrivals or P and S-wave reflections, which won't change significantly. The relatively large number of aftershocks in our study area, in comparison to regions such as the New Madrid Fault Zone or the San Andreas Fault Zone in Parkfield, could also contribute to greater changes in the Green's function on average just because the rate of movement is so high; although we are dealing with a very short time scale, the rate of land movement due to the large number of aftershocks is relatively high.

Syracuse et al. (2012) employs a similar argument to explain disparities between apparent P-wave similarity and S-wave similarity in their data set within the Christchurch fault zone. They use a similar method to ours, with a longer time window of 2.54 seconds focused around the P-wave arrival. The master trace for the methodology does not contain the S-wave, but when Syracuse et al. (2012) compare longer traces of a group of repeating events, the S-waves vary greatly despite the P-wave similarity and very similar locations given by their accurate relocations. Syracuse et al. (2012) attribute the differing

S-waves to a temporally changing structure within the ray path that would cause scattered energy to arrive at different times. Such changes would have to be affecting only the S-waves over time in order to allow the P-waves to remain similar.

Slightly Differing Focal Mechanisms

Another possibility to explain the lack of similarity in S-waves in Syracuse et al. (2012) is slightly differing focal mechanisms between the events. As we discussed earlier, the type of wave (polarity and strength) is highly dependent on the direction of propagation relative to the focal mechanism. Most importantly, because we are preferentially selecting strong P arrivals as our master traces, we would have also been preferentially selecting seismograms with weaker S arrivals (figure 7). Figure 7 makes it evident that the strongest P-wave radiation is actually the direction of zero S-wave amplitude radiation. To either side, the polarity of the S-wave will vary in opposite directions, while the amplitude of the P-wave will vary less significantly, and the polarity not at all. As a result, our method preferentially selects not only strong P arrivals, but also S arrivals that vary around zero amplitude and may fluctuate in polarity, depending only on very small changes in the relationship between the raypath and the focal mechanism. Even more interestingly, the stacked data from Syracuse et al. (2012), which should be representative of the average waveform for the repeating group, shows a strong P-wave arrival as well as a minimal S-wave arrival (figure 21). For New Zealand, in such a dynamically complex fault zone, which would cause changing stress fields since the 3 September 2010 mainshock, slightly varying focal mechanisms seem entirely within the realm of possibility. Therefore, we believe that the repeating P-signals we identify (and discovered by Syracuse et al.) are most likely caused by very similar, but still different,

focal mechanisms in about the same location, which lead to varying S-waveforms rather than pure structural changes affecting only the S-arrival.

For this interpretation of my data to work, since we would expect the similar waves to be coming out of the same part of a focal mechanism, the orientation of the focal mechanism would have to be dependent upon the location of the earthquake with respect to the station (and hence the raypath orientation). Therefore, we expect closely clustered groups to have similar focal mechanisms and more widely spread groups to have more widely differing focal mechanisms. Because the orientation and location of the focal mechanism within a group may be varying between events, it is highly unlikely that relative orientation of the focal mechanism and the raypath to the station will remain the same. As a result, the same focal mechanism in a different location would not be discovered by the second cross correlation. If this is the case, then our method is better designed to show us somewhat similar focal mechanisms within a given fault as opposed to true repeating earthquake groups.

Implications

If the Christchurch fault zone is truly not creating repeating events as our method implies, we can say a little about the fault zone given our most likely interpretation of our results, similar focal mechanisms clustered within a fault segment. Though our data set is only a partial scan of the aftershock sequence, fault segments A and G (figure 13; appendix) tended to show better clustering than the other fault segments. While these clusters don't represent true repeating earthquake families, they do imply that this section of the fault segment is slipping similarly over time. Therefore our interpretation of the

clusters could be similar to highly correlated repeating earthquakes.

These fault segments may be slipping more consistently because of a lower fault friction, possibly caused by pore pressure. Because the fault zone is complex and evolving quickly due to a large number of aftershocks, it is possible that the faulting is occurring within a wider zone that we label in our maps as a discrete fault segment with no width (figure 13). Therefore, fault segments that exhibit significant clustering, although not truly repeating earthquake families, may still represent fault segments that are less locked than those that don't. Finally, this would imply that segments A and G may be accumulating less stress build-up over time due to frequent release and would release less energy during a large rupture.

Another interesting aspect is that fault segment A is the portion of the fault zone (of those involved in the 3 September 2010 event) closest in proximity to the 21 February 2011 event. If unlocked segments cause these clusters, then increased slip rates in the on segment A may have indicated stress-loading towards the city of Christchurch and possibly rupture further eastward, which eventually happened in the form of the 21 February 2011 earthquake. Of course we have no clear evidence linking our clusters and the eventual 2011 event.

Conclusions

In this study we aimed to locate repeating earthquakes, which have been located in many other fault zones including the San Andreas Fault Zone and the New Madrid Fault Zone, by using a short window cross correlation method. The earthquakes identified by our cross correlation code are, in fact, not repeating events. However, the uniqueness of the our study area, given the region's jump from being seismically inactive to being extremely seismically active, as well as the nuances between different cross correlation methodologies has complicated the interpretations of our repeating earthquake studies. Although these issues cannot necessarily be solved given my analysis, exploring the gaps in my methodology, differences between methodologies for various repeating earthquake studies, as well as the intricacies of our study area can be enlightening to future repeating earthquake studies, especially within the region.

We do have hypotheses why repeating earthquakes might not be identifiable or occurring at all within the Darfield region. Changing Green's functions could potentially mask the earthquake source function, or our region could actually be completely lacking repeating source functions. Finally, we have the possibility that these events located by our method are well-clustered earthquakes with similar source functions, which could have implications for the fault dynamics leading up to the 21 February 2011 earthquake that devastated Christchurch.

Unfortunately, though we have given reason that the earthquakes identified by our method are not repeating, it's also possible that we could have simply missed the repeating earthquakes due to our smaller window size and higher correlation coefficient. Furthermore, there may have been repeating groups for which we never cross correlated

any of the events of the group due to our relatively small sample size of the aftershock sequence. Additionally, because of the large number of earthquakes in the aftershock sequence, most of the catalogued earthquakes were an order of magnitude larger than many of the repeating earthquake sequences recorded in other studies, which are often < M 2.0 (Bisrat et al., 2012; Chen et al., 2010). If we never chose a master trace, which was part of a repeating group, then we would never find that repeating group through cross correlation. Future repeating earthquake studies could benefit from further automation of the cross correlation process, by removing the necessity of a researcher to run the cross correlation codes individually for each event. The development of a code to eliminate the necessity of a researcher "picking" master traces or to eliminate the necessity of the aftershock catalogue completely is the only way to completely neutralize these issues.

References Cited

Anderson, M.L., and Myers, S.C., 2010, Assessment of Regional-Distance Location Calibration Using a Multiple-Event Location Algorithm: Bulletin of the Seismological Society of America, v. 100, no. 2, p. 868-875.

Beavan, J., Samsonov, S., Motagh, M., Wallace, L., Ellis, S., and Palmer, N., 2010, The Darfield (Canterbury) Earthquake: Geodetic Observations and Preliminary Source Model: Bulletin of the New Zealand Society for Earthquake Engineering, v. 43, no. 4, p. 228.

Bisrat, S., DeShon, H.R., and Rowe, C., 2012, Microseismic Swarm Activity in the New Madrid Seismic Zone: Bulletin of the Seismological Society of America, v. 102, no. 3, p. 1167.

Chen, K.H., Nadeau, R.M., and Rau, R., 2007, Towards a universal rule on the recurrence interval scaling of repeating earthquakes?: Geophysical Research Letters, v. 34, no. 16, p. L16308.

Chen, K.H., Buergmann, R., Nadeau, R.M., Chen, T., and Lapusta, N., 2010, Postseismic variations in seismic moment and recurrence interval of repeating earthquakes: Earth and Planetary Science Letters, v. 299, no. 1-2, p. 118-125.

Davies, T., Otago Regional Council, 2007, Great Alpine Fault earthquake talks: http://www.orc.govt.nz/Information-and-Services/Natural-Hazards/Great-Alpine-Fault-Earthquake/ (4/18 2013).

Eberhart-Phillips, D., Reyners, M., Bannister, S., Chadwick, M., and Ellis, S., 2010, Establishing a Versatile 3-D Seismic Velocity Model for New Zealand: Seismological Research Letters, v. 81, no. 6, p. 992-1000.

Elliott, J.R., Nissen, E.K., England, P.C., et al., 2012, Slip in the 2010–2011 Canterbury earthquakes, New Zealand: Journal of Geophysical Research, v. 117.

GeoNet, GeoNet, 2013, Quake Search: http://magma.geonet.org.nz/resources/quakesearch/ (4/17 2013).

GNS Science, GNS Science, 2/25/2011, 6.3 magnitude earthquake part of aftershock sequence: http://www.gns.cri.nz/Home/News-and-Events/Media-Releases/earthquake-part-of-aftershock-sequence (4/16 2013).

Holden, C., Beavan, J., Fry, B., et al., 2011, Preliminary source model of the Mw 7.1 Darfield earthquake from geological, geodetic and seismic data: Proceedings of the Ninth Pacific Conference on Earthquake Engineering.

Lillie, A.R., 1980, Strata & Structure In New Zealand: Auckland, NZ, Tohunga, 441 p.

Lillie, R.J., 1999, Whole Earth Geophysics: An Introductory Textbook for Geologists and Geophysicists: Upper Saddle River, NJ, Prentice Hall, 361 p.

Long, H., and Wen, L., 2012, Using repeated sources to quantitatively determine temporal change of medium properties: Theory and an example: Journal of Geophysical Research-Solid Earth, v. 117, p. B09303.

MacCarthy, J. K., C. A. Rowe (2005), Automatic scanning detection for characterization of dome-related seismic swarms at Mount St. Helens, and their evolution through time, EOS, Transactions, AGU, Fall Meet. Suppl. 86(52), V53D-1591.

Nadeau, R.M., Foxall, W., and McEvilly, T.V., 1995, Clustering and Periodic Recurrence of Microearthquakes on the San Andreas Fault at Parkfield, California 267, 503 p.

NZPA, http://www.stuff.co.nz/national/christchurch-earthquake/4780793/Christchurch-earthquake-death-toll-reaches-182, 2011, Christchurch earthquake death toll reaches 182: www.stuff.co.nz (4/18 2013).

Quigley, M., Villamor, P., Furlong, K., et al., 2010, Previously Unknown Fault Shakes New Zealand's South Island: Eos, Transactions American Geophysical Union, v. 91, no. 49, p. 469-470.

Rowe, C.A., Aster, R.C., Borchers, B., and Young, C.J., 2002, An automatic, adaptive algorithm for refining phase picks in large seismic data sets: Bulletin of the Seismological Society of America, v. 92, no. 5, p. 1660-1674.

Stein, S., and Wysession, M., 2003, An Introduction to Seismology, Earthquakes, and Earth Structure: Malden, MA, Blackwell Publishing, 498 p.

Syracuse, E.M., Holt, R.A., Savage, M.K., et al., 2012, Temporal and spatial evolution of hypocentres and anisotropy from the Darfield aftershock sequence: implications for fault geometry and age: New Zealand Journal of Geology and Geophysics, v. 55, no. 3, p. 287-293.

Waldhauser, F., and Ellsworth, W., 2000, A double-difference earthquake location algorithm: Method and application to the northern Hayward fault, California: Bulletin of the Seismological Society of America, v. 90, no. 6, p. 1353.

Wallace, L.M., Beavan, J., McCaffrey, R., Berryman, K., and Denys, P., 2007, Balancing the plate motion budget in the South Island, New Zealand using GPS, geological and seismological data: Geophysical Journal International, v. 168, no. 1, p. 332-352.

West, M., 2007, GI Seismology Matlab Objects: GISMO.

Yamashita, Y., Shimizu, H., and Goto, K., 2012, Small repeating earthquake activity, interplate quasi-static slip, and interplate coupling in the Hyuga-nada, southwestern Japan subduction zone: GEOPHYSICAL RESEARCH LETTERS, v. 39.

Zhang, H., and Thurber, C.H., 2003, Double-difference tomography: The method and its application to the Hayward Fault, California: Bulletin of the Seismological Society of America, v. 93, no. 5, p. 1873.

Figures

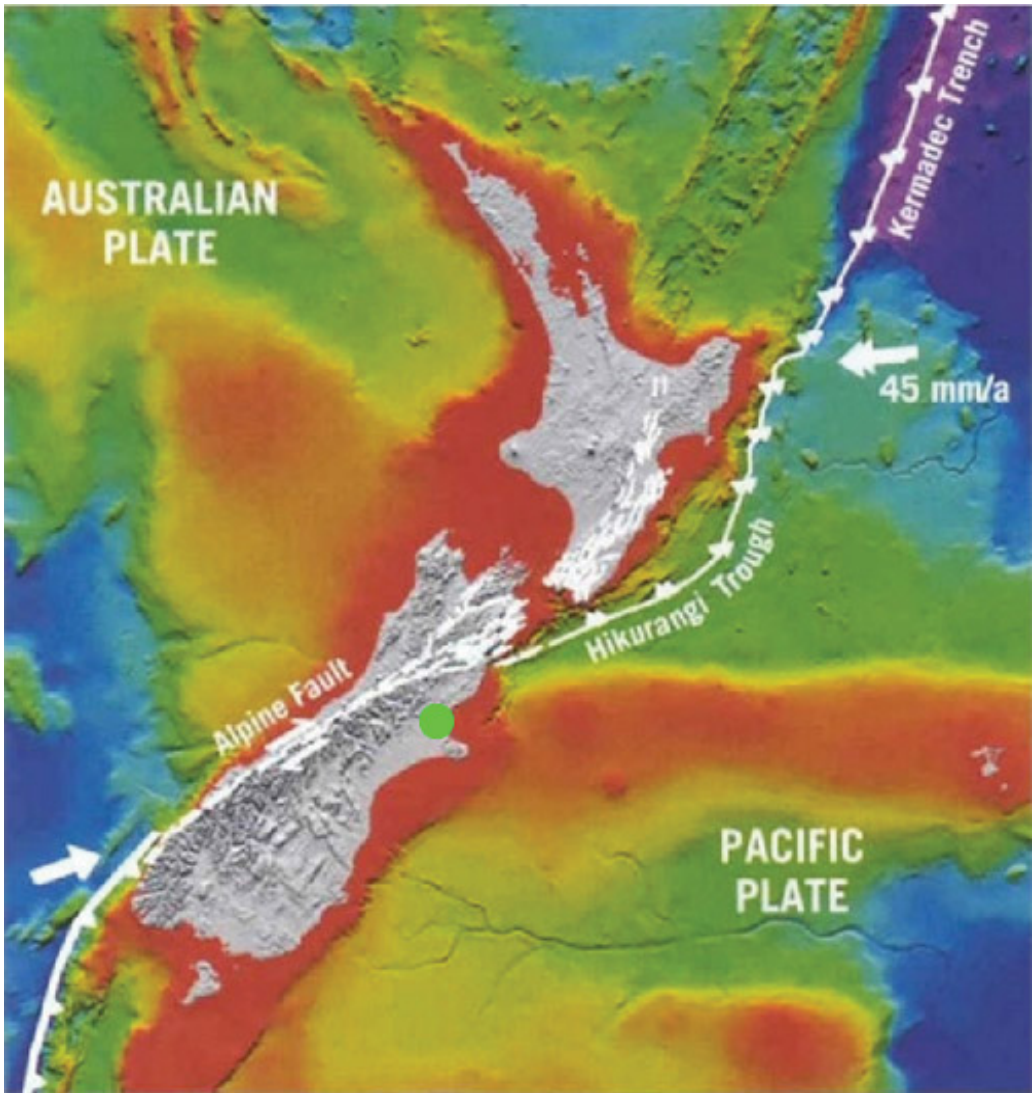

Figure 1 – This figure is a bathymetric map of New Zealand with the warmer colors representing shallower areas and the cooler colors representing deeper areas. New Zealand is tectonically complex with westward subduction of the Pacific Plate under the Australian Plate at a rate of 45 mm/yr in the north and eastward subduction of the Australian Plate under the Pacific Plate to the south. There is a zone of right-lateral strike-slip motion along the Alpine fault and other fault strands in between. The green circle represents the Darfield plains and Christchurch along the coast. Image modified from Davies (2007).

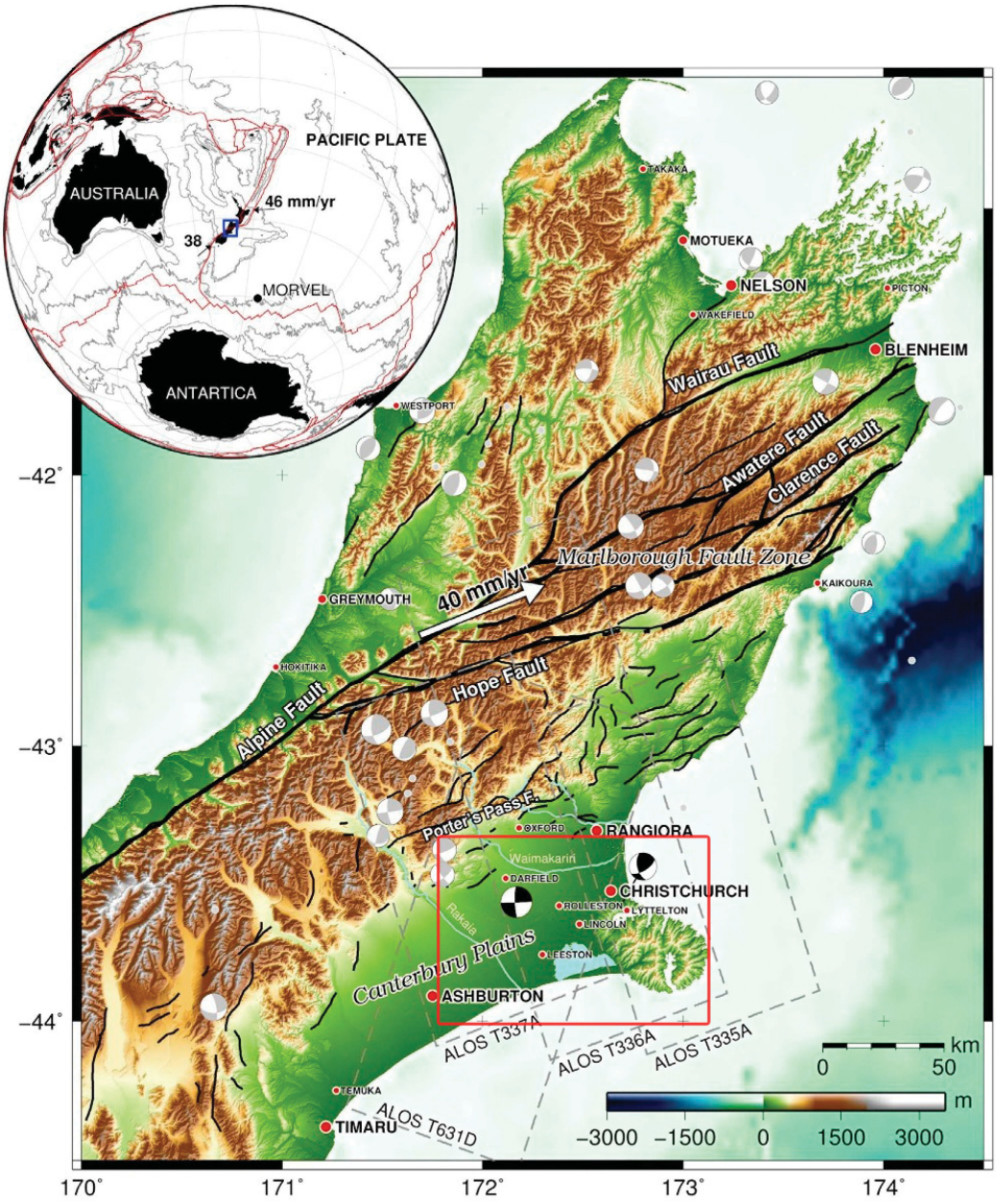

Figure 2 – The inset in the upper left puts New Zealand into global tectonic context. Red lines represent plate boundaries while black represents continents. The subduction zones to the north and south of the South Island are subducting at rates of 45 mm/yr and 38 mm/yr respectively. The blue box represents the location of the rest of the figure. The main map shows the topographic relief of New Zealand along with the fault segments within the Southern Alps that compose the New Zealand Shear Belt (NZSB), including the Alpine Fault and other fault strands. Some faults are found as far south as the Northern Canterbury Plains. The Banks Peninsula extends southeast from Christchurch. Black focal mechanisms represent the Darfield and Christchurch earthquakes, while gray and white focal mechanisms represent historic earthquakes. The red box represents our study area and is shown in figure 3. (Elliott

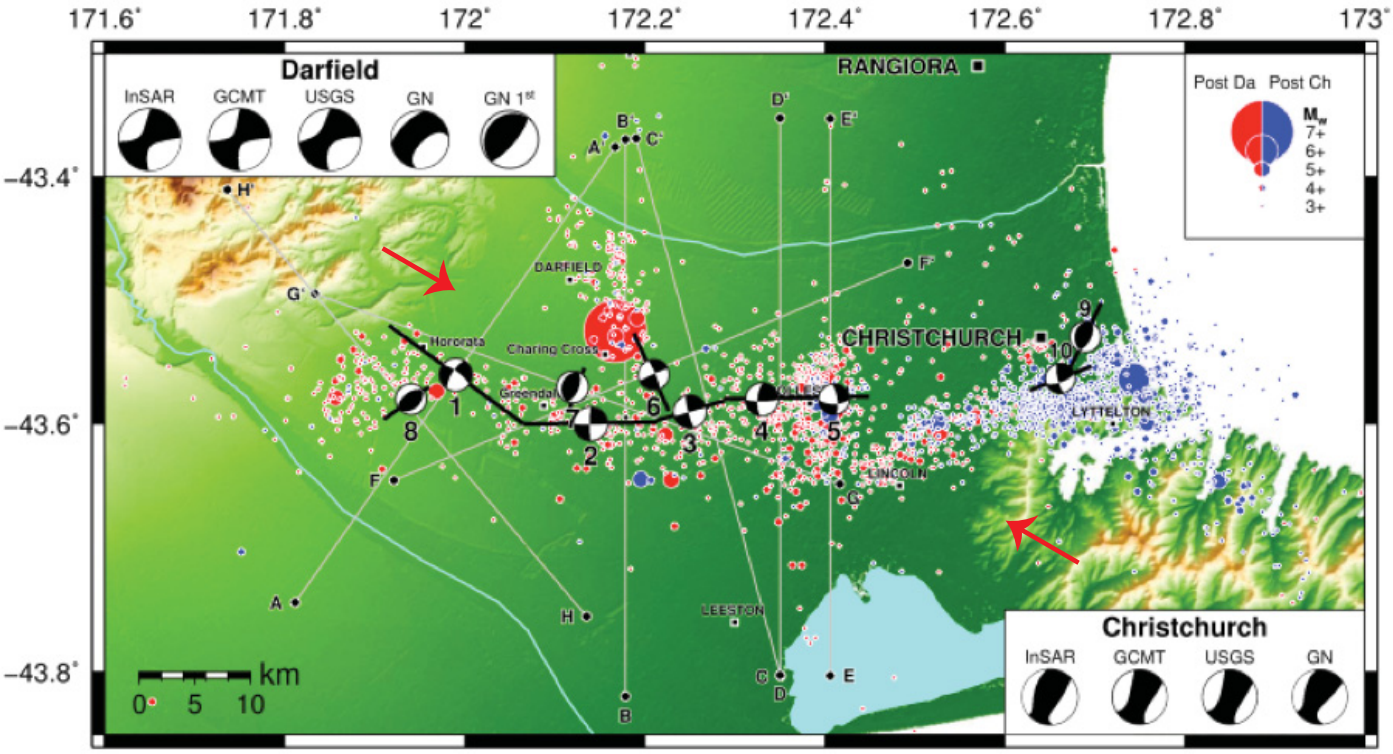

Figure 3 – A map view of the fault complex modeled by Elliott et al. (2012) along with focal mechanisms for the individual fault segments. Red and blue circles designate all aftershocks and mainshocks of the September 2010 (Darfield) and February 2011 (Christchurch) events respectively. The various focal mechanisms are various solutions from both the USGS and GNS for the Christchurch and Darfield earthquakes. Note the strip of seismicity indicated by the red dots extending northward in the direction of fault segment 6. Note the very high rates of seismicity near fault segment 5. The red arrows represent the calculated contraction direction within the region from Wallace et al. (2007) at 120 degrees from North.

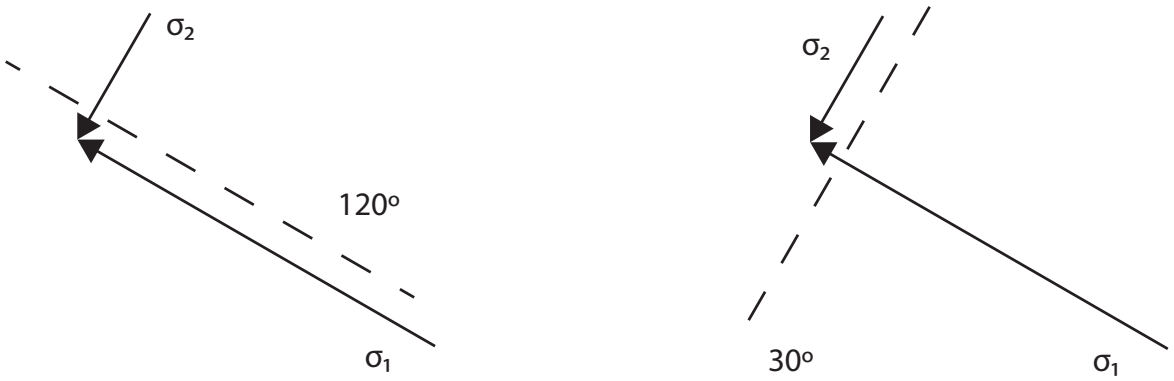

Figure 4 - This figure shows 2 of 3 orthogonal basis vectors, which represent the stress field acting on a plane. The length of the arrows is representative of the stress magnitude. Note that if σ_3 were pictured it would be pointing directly into the paper and would be smaller than σ_1 and σ_2. Two fault planes (dotted lines) oriented at 120° and 30° east of north contain σ_1 and σ_2 respectively. It is clear that the normal stress is larger on the fault plane oriented 30° east of north because the perpendicular stress is larger.

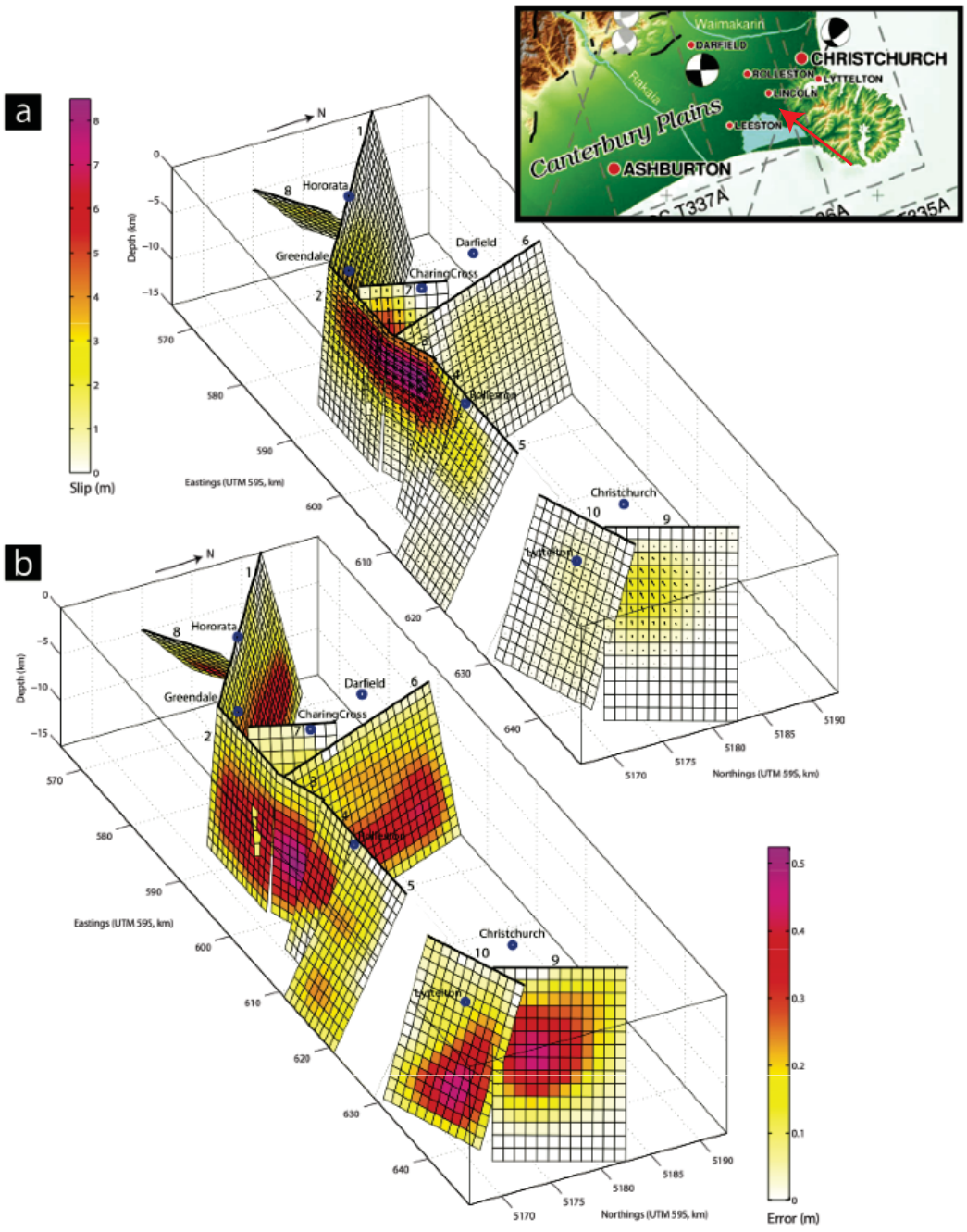

Figure 5 - Model from Elliott et al. (2012), which shows the slip for the 3 September 2010 event on fault segments 1-8 as well as the 21 February 2011 on fault segments 9 and 10. The top right box is a map view of the same area with Christchurch and Darfield labeled. The red arrow on the inset map indicates the direction of view for the rest of the figure. The rupture initiated on the SE dipping thrust fault, number 7, but the majority of the slip was right-lateral and occurred on fault segments 2, 3, and 4, with a maximum slip of 8.0 m. Minimal slip was recorded on the NS-trending left lateral fault segment 6. Part A of the figure represents the amount of slip on each fault plane, while B represents the error associated with the slip model.

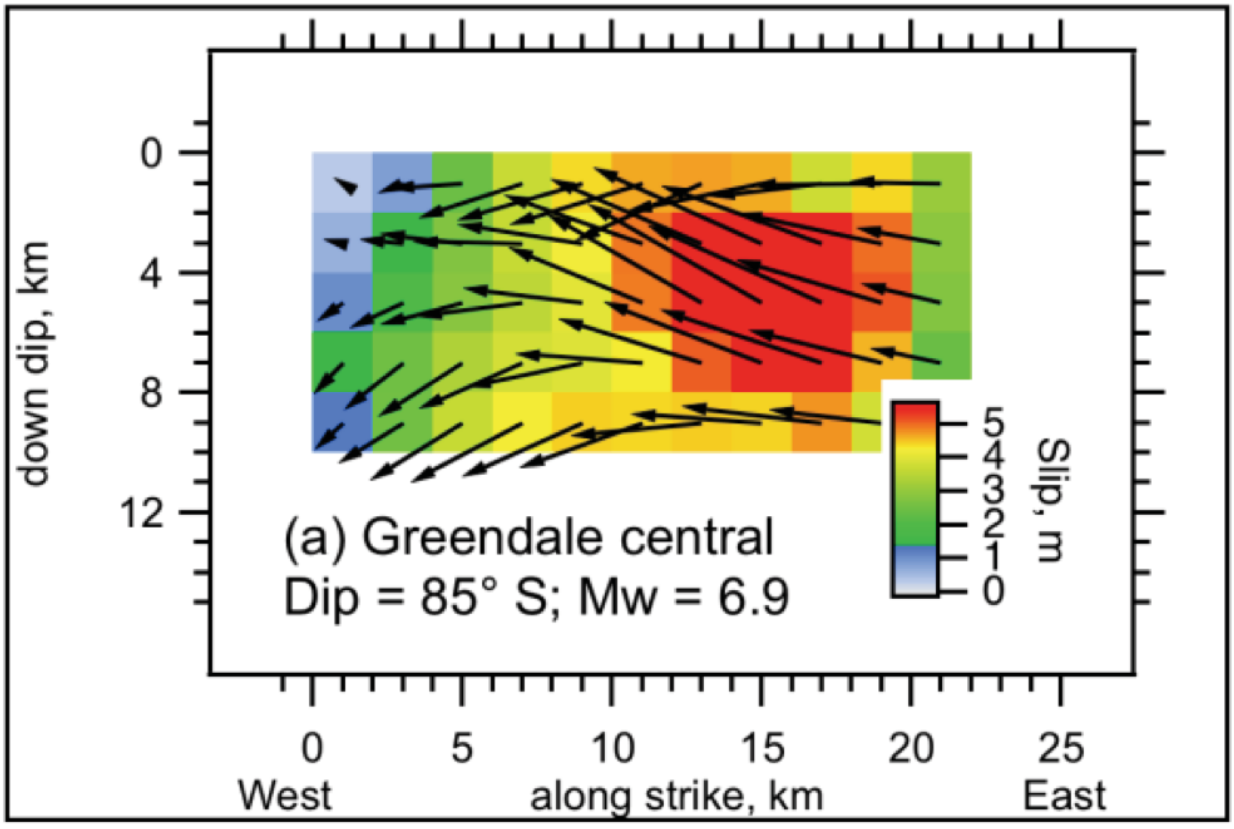

Figure 6 – This slip model from Beavan et al. (2010) shows the motion of the hanging wall relative to the footwall on fault segment 2 (figure 4). The colors represent the slip magnitude in meters while the arrows represent direction of motion.

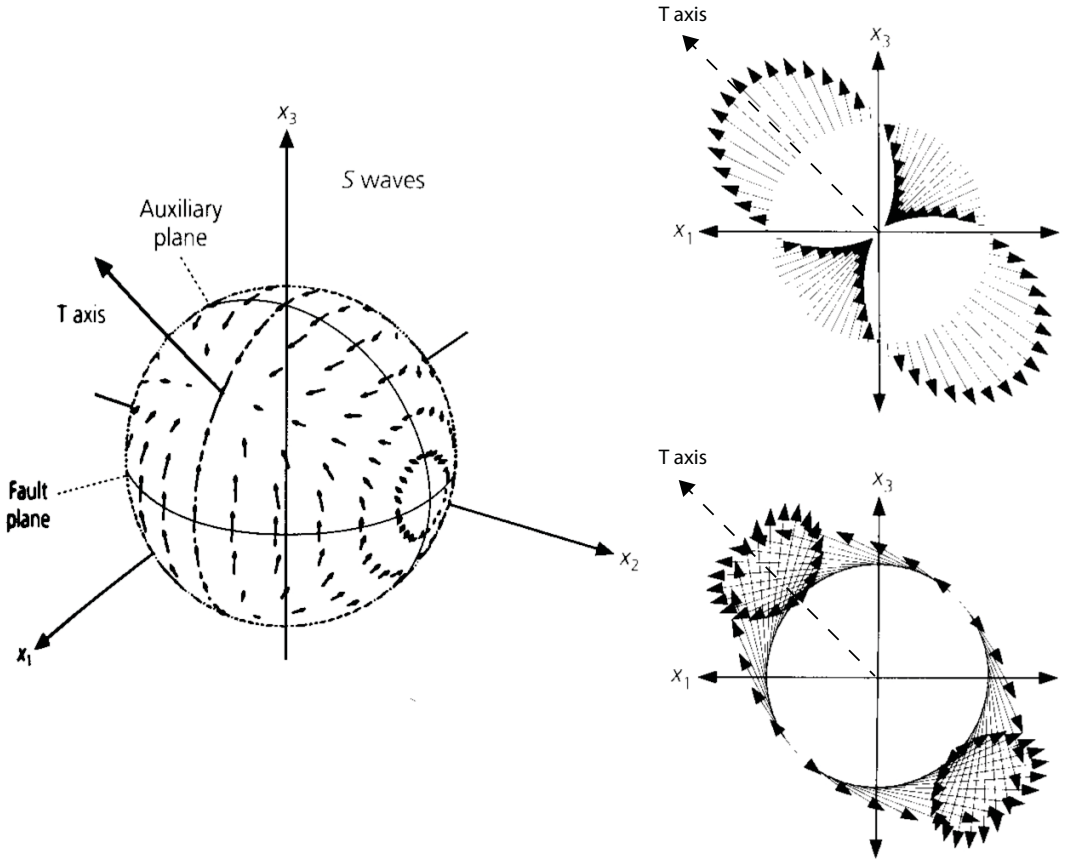

Figure 7 – These three figures represent wave radiation patterns. The fault plane for these 3 images lies within the x_1 and x_2 axes. Therefore, in the 2-dimensional representations, the fault plane lies along x_1 only. The T-axis bisects x_1 and x_3 but lies within the plane of the x_1 and x_2 axes. The left and bottom right images represent shear (S) wave radiation pattern, while the upper right image represents the compressional (P) wave radiation pattern. Along the x_1 and x_3 axes the s waves are at their strongest and the P-waves are zero. Conversely, along the T-axis we get the strongest P-waves and zero amplitude S-waves. As we move across the T-axis, we see only slight directional and magnitude changes in P-waves, while we see relatively larger magnitude changes in S and a polarity (or sign) shift across the axis. Because our method preferentially chooses strong P-wave arrivals, we tend to be choosing waveforms created along the T-axis of focal mechanisms. (Stein and Wysession, 2003)

Figure 8 – Schematic raypath diagram. The stars represent seismic events while the triangle and horizontal line represent the earths surface and a seismic station and the curved lines show the raypaths to the station. Immediately after an earthquake, seismic waves travel outward in all directions and reflect and refract off of different layers. However, this figure shows first arrival of an earthquake wave at a given seismic station, which takes the most direct path to a seismic station. This raypath for this wave takes the fastest path from the source to the station. Because velocity tends to increase with depth due to increasing pressure and density, raypaths curve upward toward the surface. Notice that two different raypaths pass through different parts of the earth, which may change the seismic signal at the station even if the source signals are the same.

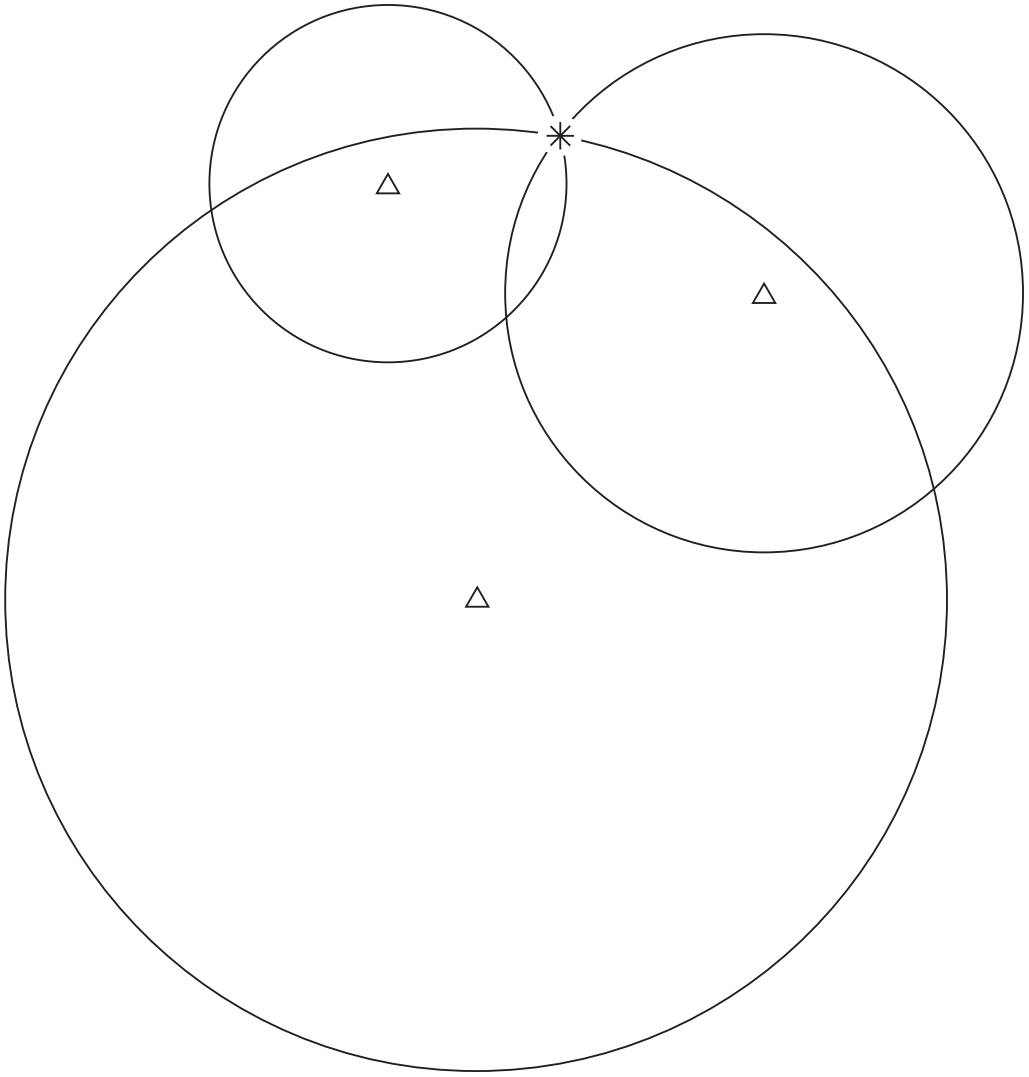

Figure 9 – Schematic diagram of earthquake location. If the S-wave and P-wave velocities are known for a region, then we can use the difference of the two arrival times to calculate a radial distance X that the source is from the station as in equation 6. Thus we can draw a circle with radius centered on the seismic station. If the same is done at two more stations, the result will show the map view location of the seismic source (epicenter). The star represents the true location of the earthquake, while the triangles represent seismic stations that identified first arrivals and the circles represent the distance of the epicenter from each station.

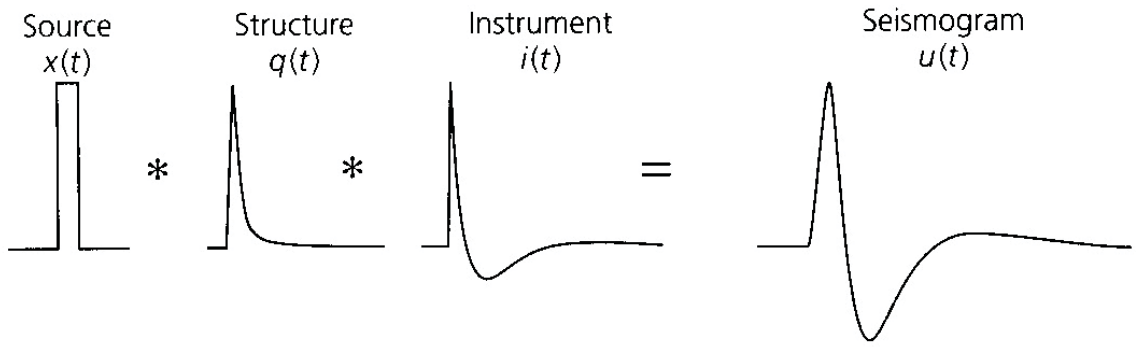

Figure 10 - A seismogram is a mathematical combination (convolution, designated by an asterisk) of the source function [(x(t)], the structure [or the Green's function, q(t)], and the instrument response [i(t)] (Stein and Wysession, 2003).

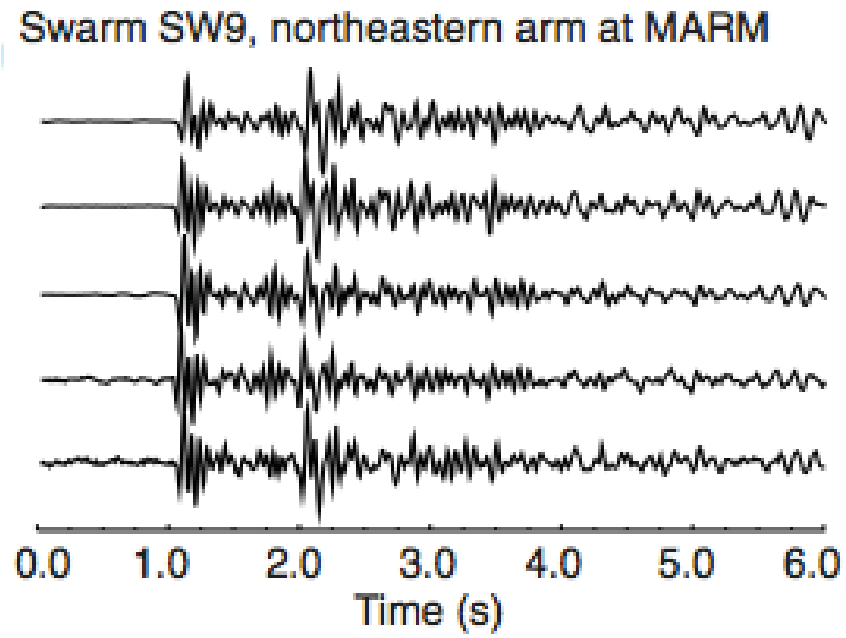

Figure 11 - This swarm of small repeating earthquakes, from Bisrat et al. (2012), have similarity coefficients of 0.80 or more for each event. SW9 is the name of the swarm occurring at the northeastern arm of the New Madrid Fault Zone. These traces were all recorded at different times from different earthquakes from the same swarm at the seismic station MARM. We can clearly see the P-wave and S-wave arrivals at 1.0 and 2.0 seconds respectively.

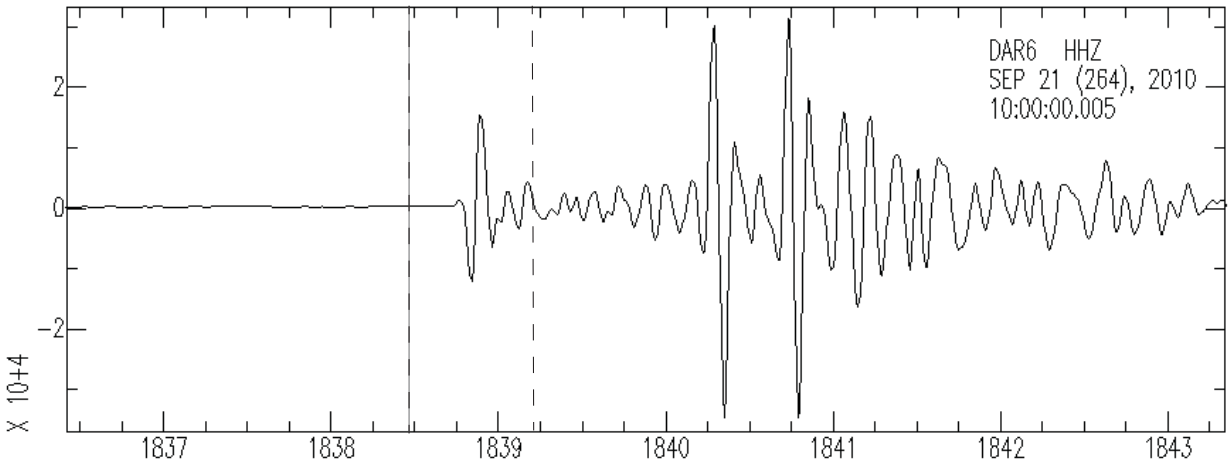

Figure 12 – This figure shows the full waveform of the master event for group 4, our most spatially clustered group. Our cross correlation method only used 0.3 seconds before and 0.4 seconds after the P-arrival in the seismogram (the dashed lines). The horizontal axis is in seconds and the vertical axis shows counts of ground motion.

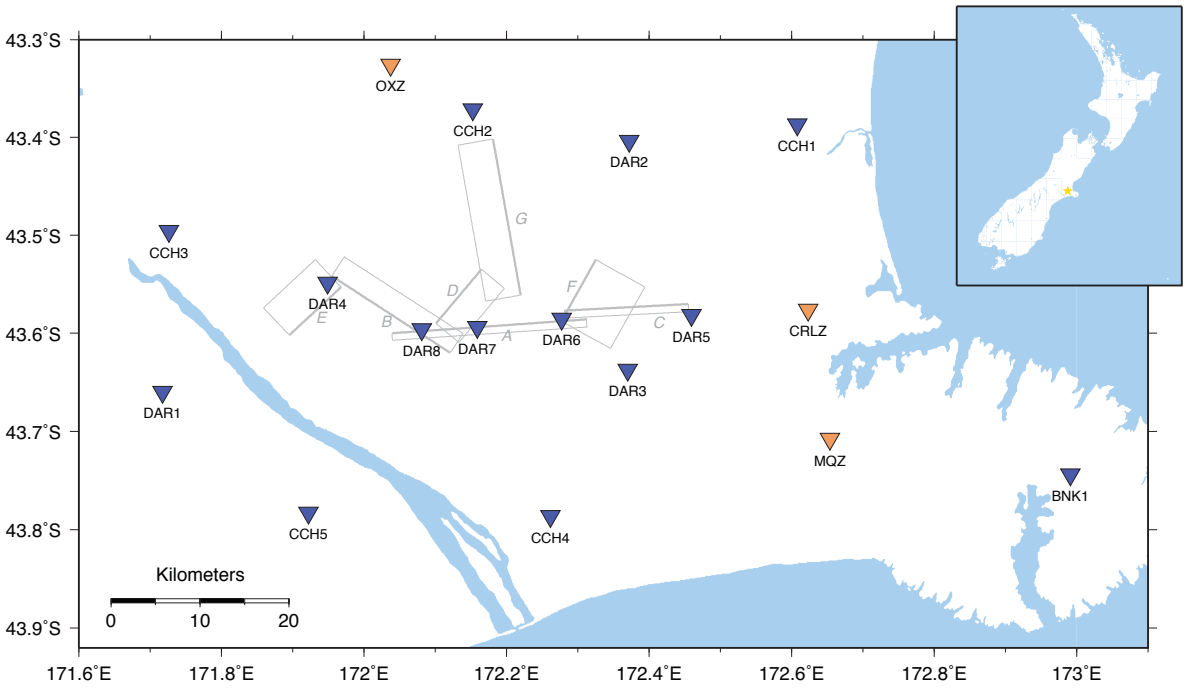

Figure 13 – This is the station map for our field area. The upper right inset features a gold star, which puts the field area into regional context. Triangles represent the seismic stations. Orange stations are permanent stations from the region and were already present before the 4 September 2010 event, while blue stations were deployed by the University of Wisconsin-Madison and Victoria University a few days after the 2010 mainshock. The gray boxes represent the fault segments taken from Elliot et al. (2012). Thicker gray lines represent the fault location at the surface while the other lines indicate the fault plane below the surface. Therefore, narrower boxes relate to more vertical fault planes.

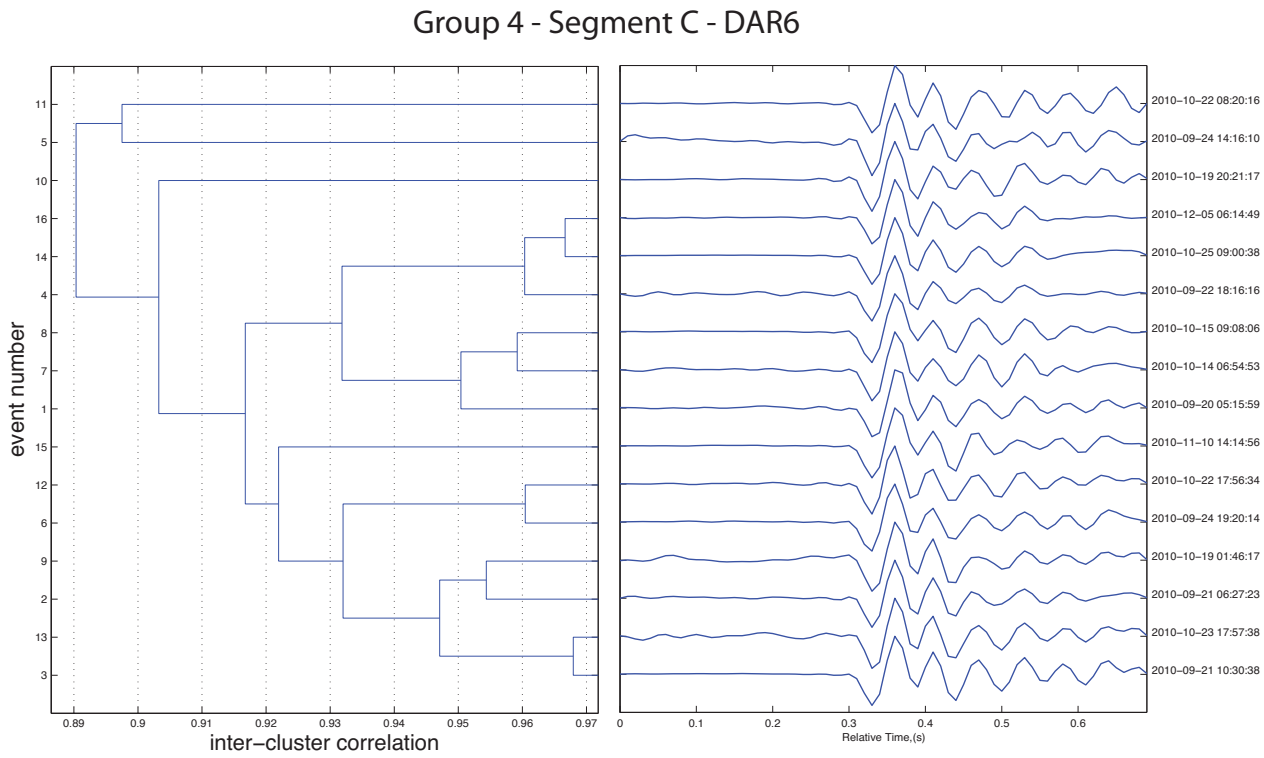

Figure 14 - GISMO (West, 2007) organizes the seismic traces of our potentially repeating events from one station in a hierarchical tree. The left section of the figure represents the seismic trace of a group, which our cross correlation code recognized as potential repeating earthquakes. The right side of the figure shows these seismic traces based on their similarity coefficients. Any two traces that are connected by a vertical line in the inter-cluster correlation graph correlate to the value specified on the horizontal axis. This chart represents the group is our most likely potential repeating earthquake group. We can see that all but the top two traces correlate to 0.9 or better. Figure 13 defines segment names.

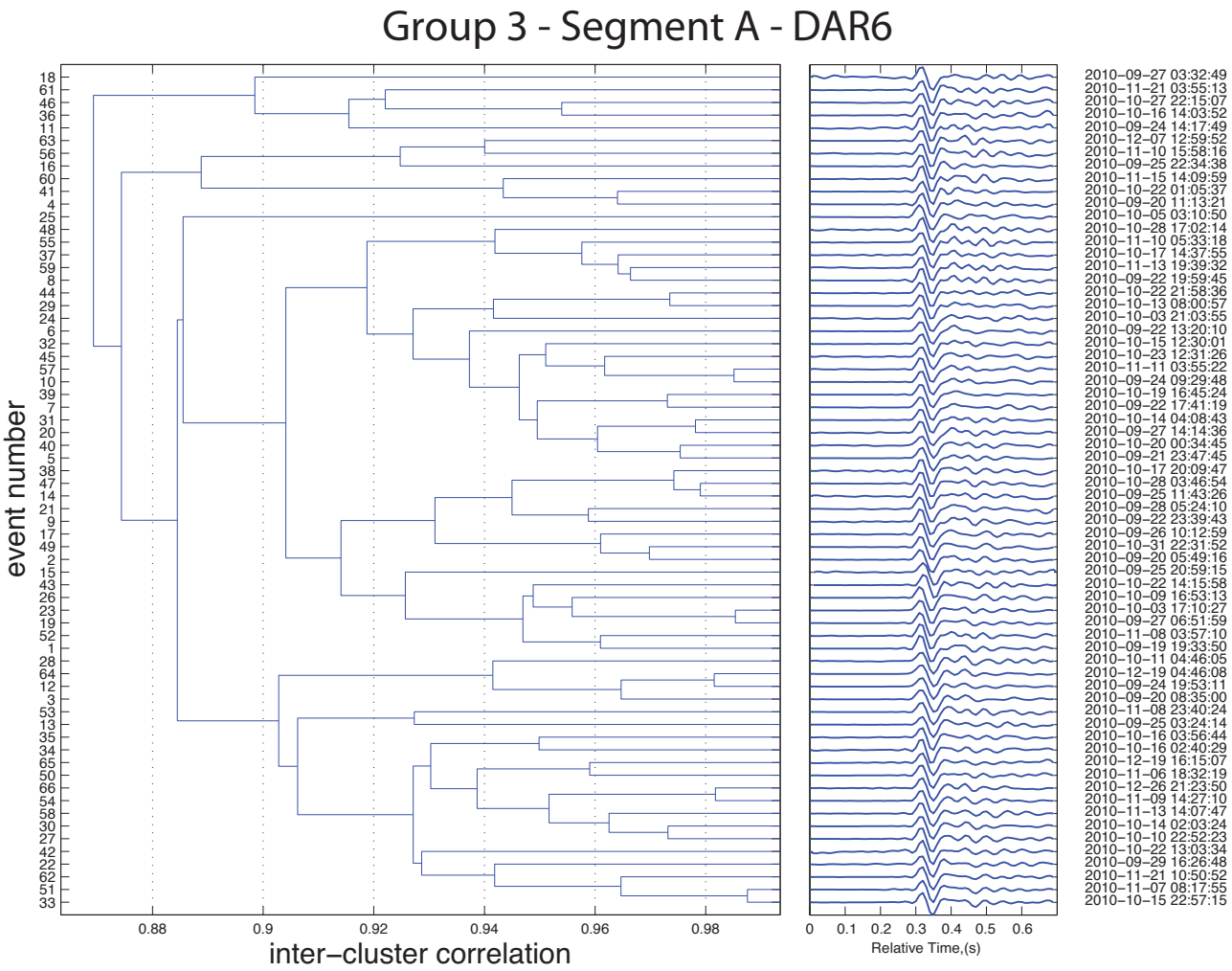

Figure 15 – This figure is a Gismo plot similar (with the same axes) to that in figure 14. This chart represents our largest potential repeating earthquake group. We can see overall the correlation is not as strong as it is for Group 4. Figure 13 defines segment names.

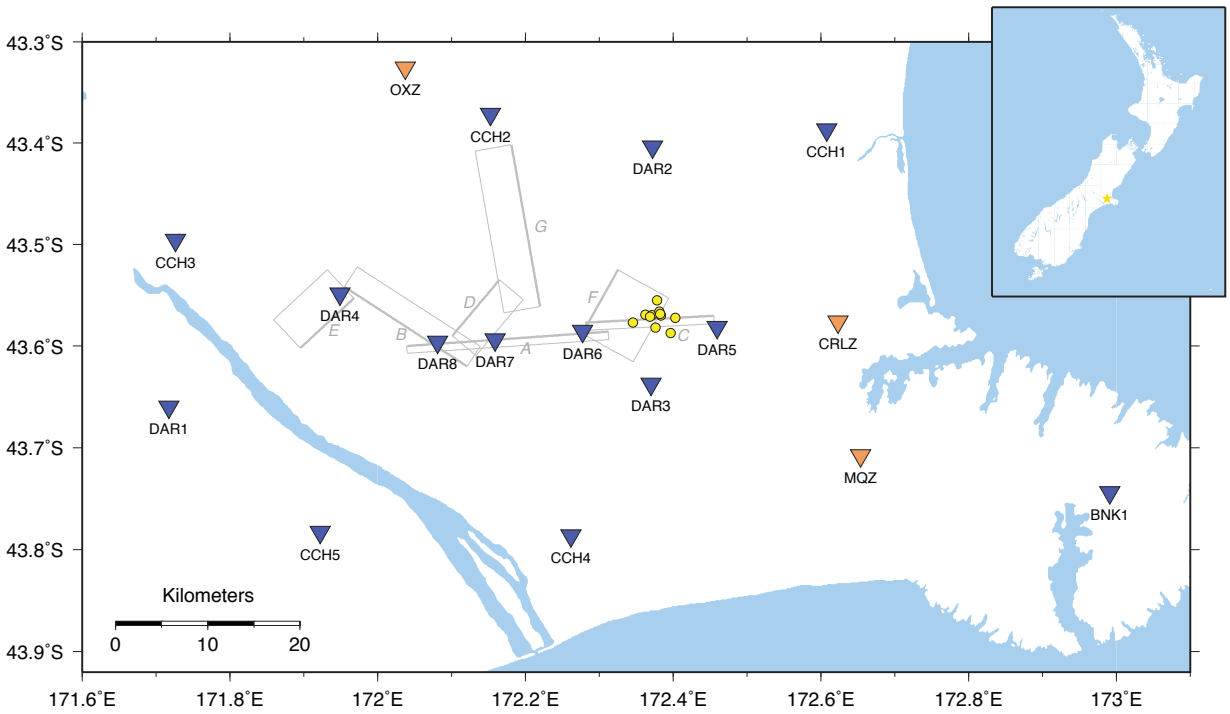

Figure 16 – Each circle is an earthquake location from potential repeating earthquake Group 4. Note how well clustered the events are, possibly alongthe fault segment C since that was the origin of the master trace. All events fall within 5-10 km depth, indicated by their color. We took the master trace for Group 4 from DAR6.

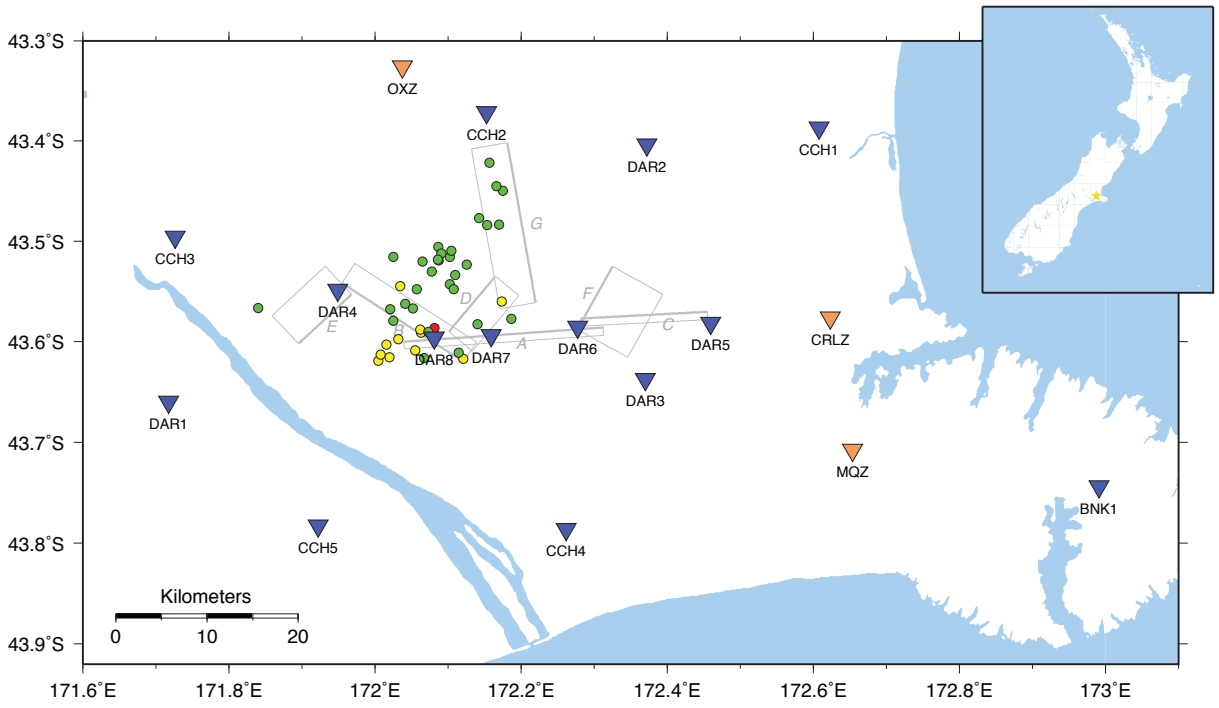

Figure 17 – Each circle is an earthquake location from potential repeating earthquake group 6. Location depths of 0-5 km are red, 5-10 km are yellow, and 10-15 km are green. Note the very poor clustering of events both laterally and with depth. Although the master trace originated on fault segment A, most of the locations are not anywhere near A. This is strong evidence that these earthquakes are not repeating events.

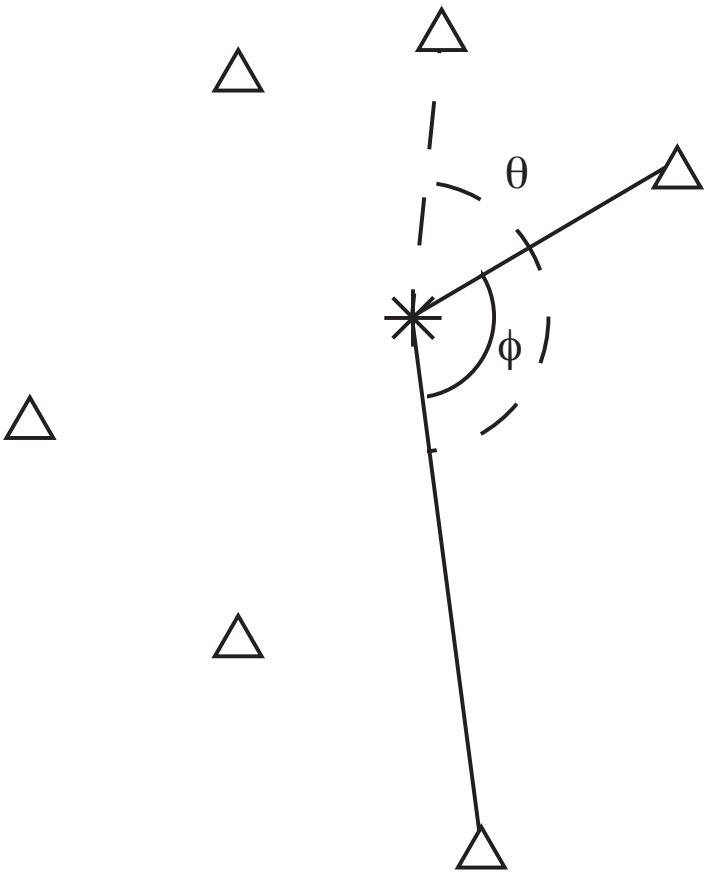

Figure 18 – Schematic diagram of azimuthal gaps. The azimuthal gap is defined by the largest number of degrees between two adjacent stations and secondary azimuthal gap by the largest gap between two stations with one in between. In this diagram, the solid lines and ϕ represent the azimuthal gap, while the dashed lines and θ represent the secondary azimuthal gap. The straight lines represent the raypath from the event (star) to the seismic stations (triangles) in map view.

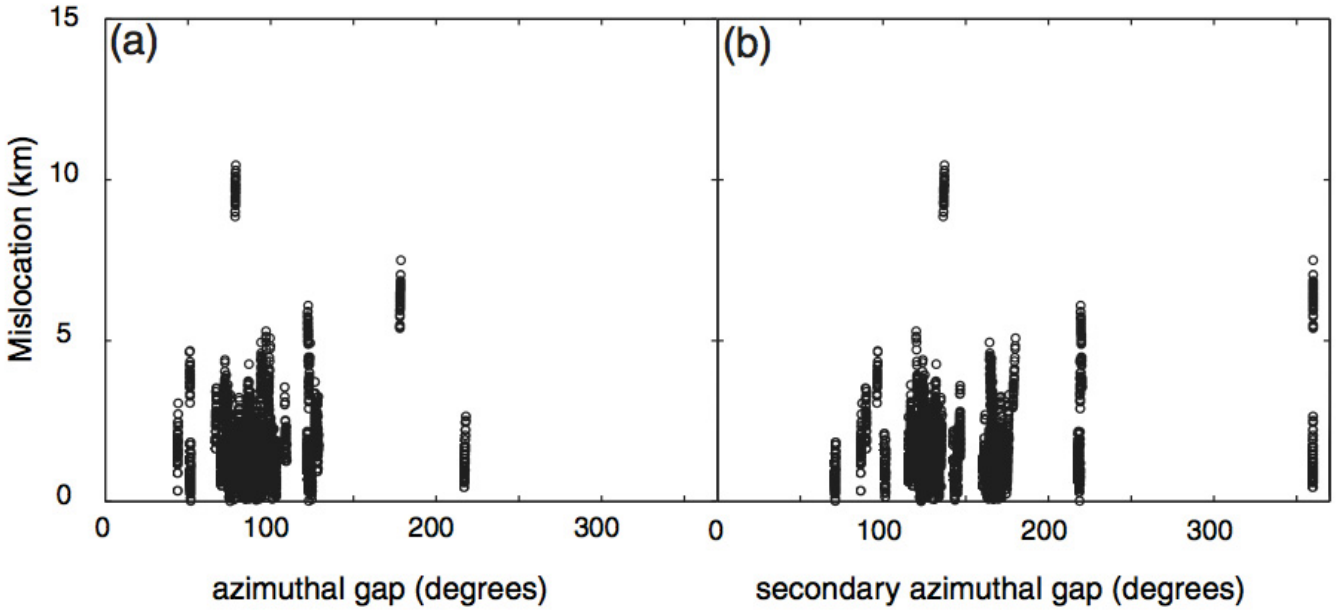

Figure 19 - This graph from Anderson and Myers (2010) shows correlation between the primary and secondary azimuthal gap and mislocation. Note the general lack of correlation between increasing azimuthal gap and the mislocation. Anderson and Myers attribute this to utilizing a multiple event location method.

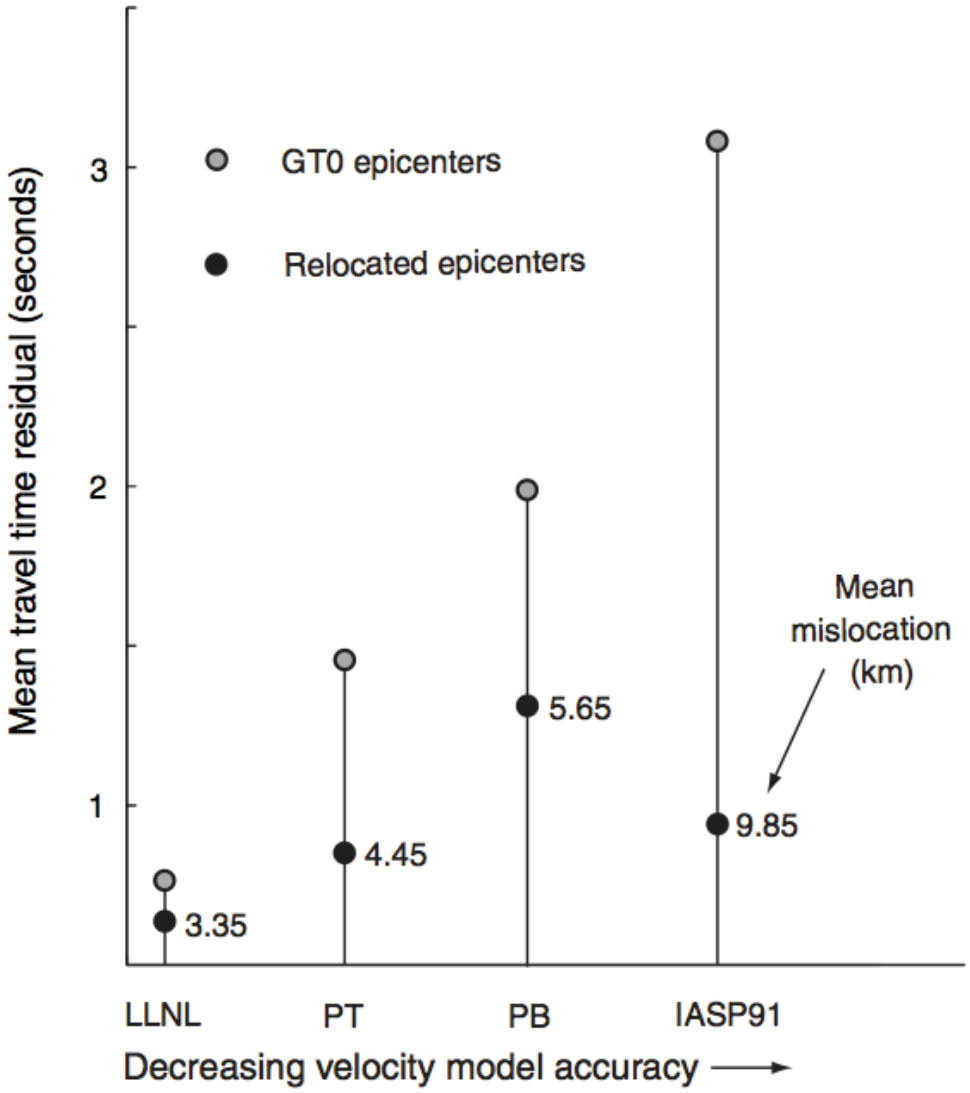

Figure 20 – This figure illustrates the relationship between various models velocity and their reported errors for locating nuclear tests with known locations. The models consist of three regional models (LLNL, PT, and PB) as well as one global model (IASP91). The multiple-event locator uses each velocity model to calculate a reported time residual as well as a location. The actual time residual errors of the GT0 epicenter are a function of the velocity model used to calculate the location. We can see that although the global model is the least accurate velocity model, with both the highest mislocation and the highest actual time residual, it actually reports a lower time residual than the PB velocity model. (Anderson and Myers, 2010)

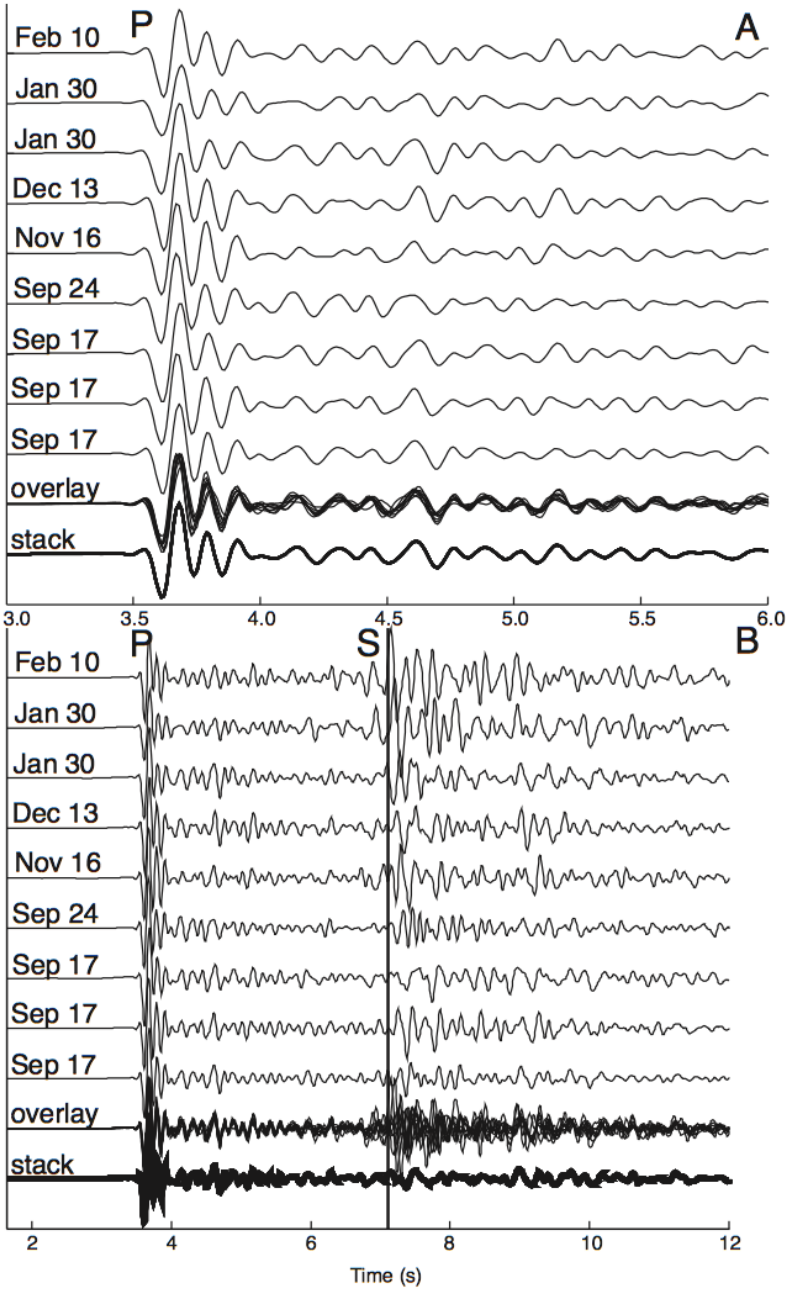

Figure 21 – This figure from Syracuse et al. (2012) shows a potential repeating family within the aftershock sequence from our study area. Syracuse defined her repeating earthquakes as events with a 0.95 correlation coefficient at two or more stations. The top of the figure shows the cross correlated waveforms, and the bottom shows a longer seismic trace of the repeating events including the s arrival. Interestingly, the S-waves are not repeating between waveforms. Because the method involves picking strong P-wave arrivals, we might expect to see lots of S-wave variation caused by slightly different focal mechanisms as shown in figure 7. If the focal mechanisms vary we would expect the S-waves that reach the same station to radiate out of slightly different places that are close to the T-axis. Thus we would expect to have an average S-wave amplitude of zero. Syracuse's data shows a stack (average) of all of the waveforms with a very strong P-arrival, but an almost non-existent S-wave arrival. This might indicate that these highly similar earthquakes have slightly differing focal mechanisms that cause minimal changes in P-wave radiation, but larger relative changes in S-wave radiation.

Appendix

The appendix shows the gismo plots similar to figures 14 and 15 as well as the earthquake location plots similar to figures 16 and 17 for all 9 of the potential repeating family groups.

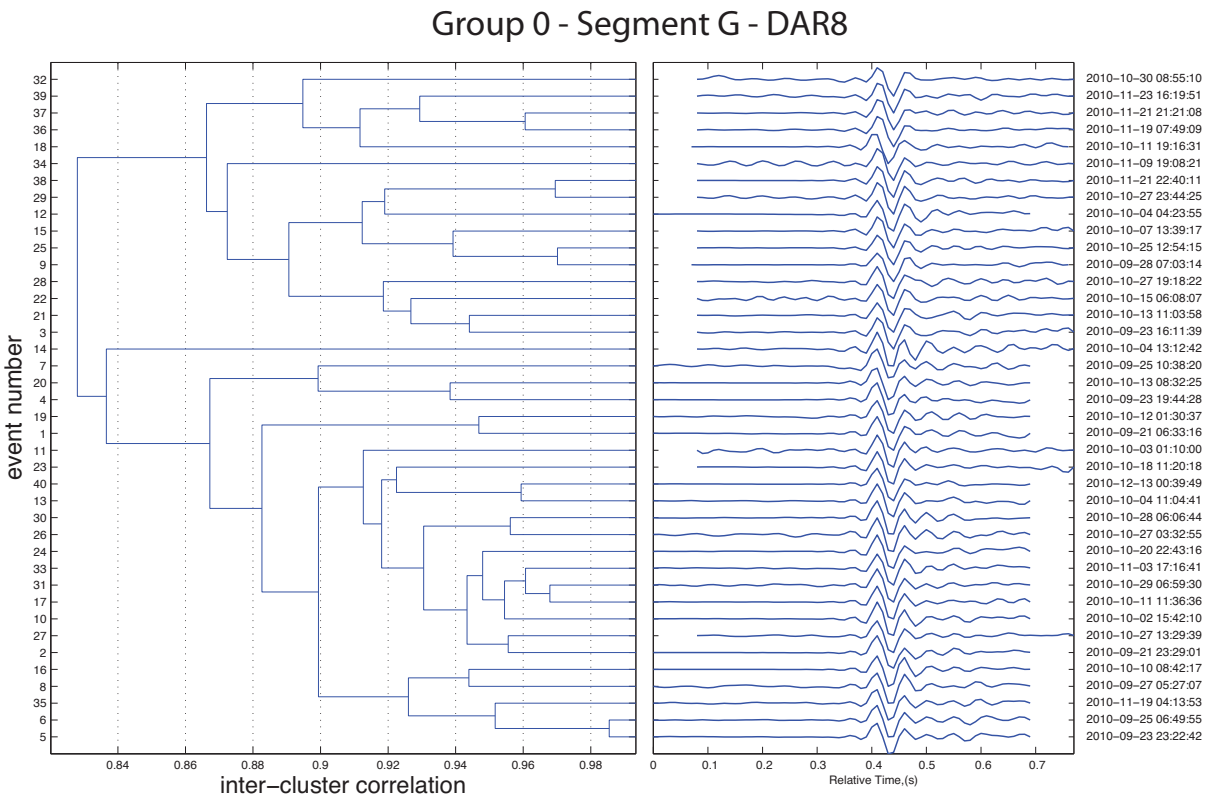

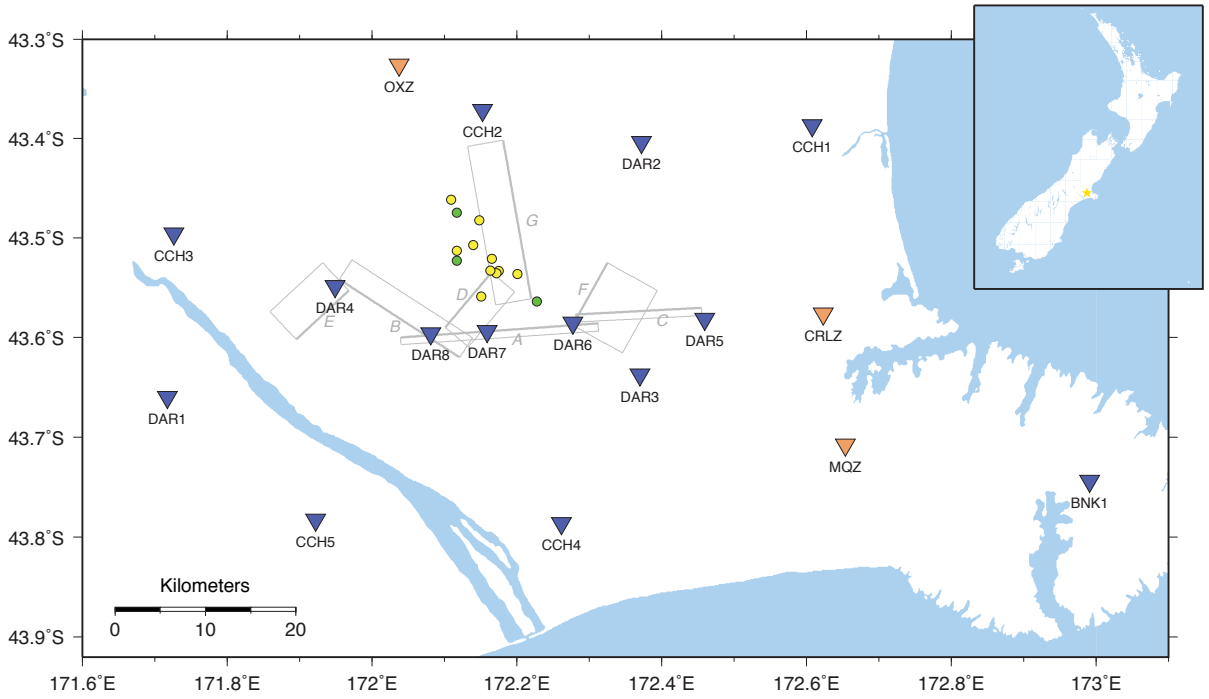

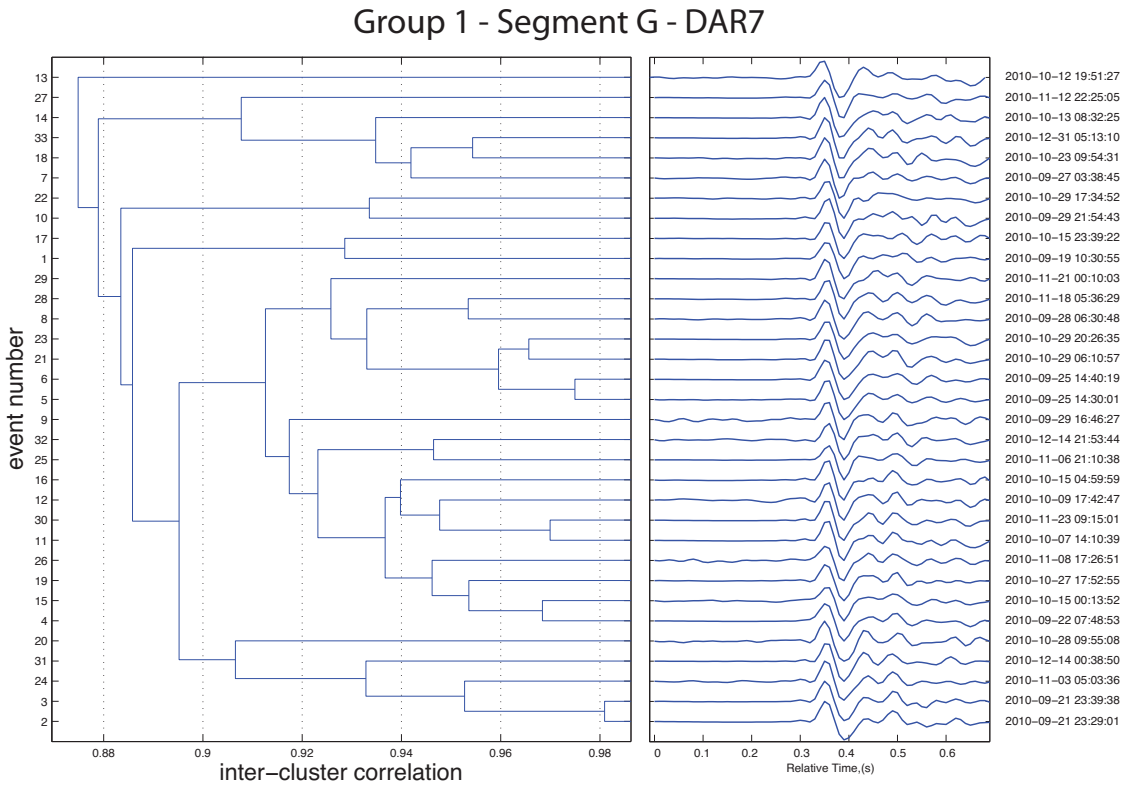
Group 1 - Segment G - DAR7
event number
inter–cluster correlation
Relative Time,(s)
2010–10–12 19:51:27
2010–11–12 22:25:05
2010–10–13 08:32:25
2010–12–31 05:13:10
2010–10–23 09:54:31
2010–09–27 03:38:45
2010–10–29 17:34:52
2010–09–29 21:54:43
2010–10–15 23:39:22
2010–09–19 10:30:55
2010–11–21 00:10:03
2010–11–18 05:36:29
2010–09–28 06:30:48
2010–10–29 20:26:35
2010–10–29 06:10:57
2010–09–25 14:40:19
2010–09–25 14:30:01
2010–09–29 16:46:27
2010–12–14 21:53:44
2010–11–06 21:10:38
2010–10–15 04:59:59
2010–10–09 17:42:47
2010–11–23 09:15:01
2010–10–07 14:10:39
2010–11–08 17:26:51
2010–10–27 17:52:55
2010–10–15 00:13:52
2010–09–22 07:48:53
2010–10–28 09:55:08
2010–12–14 00:38:50
2010–11–03 05:03:36
2010–09–21 23:39:38
2010–09–21 23:29:01

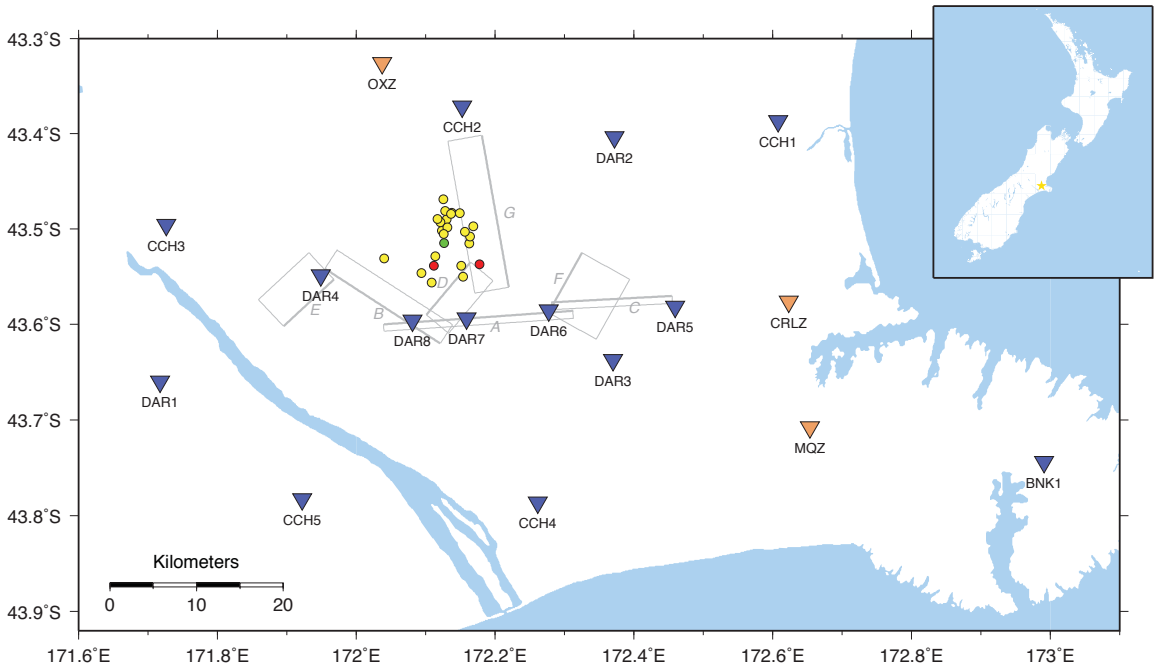
OXZ
CCH2
DAR2
CCH1
CCH3
DAR4
DAR8
DAR7
DAR6
DAR5
DAR3
DAR1
CRLZ
MQZ
BNK1
CCH5
CCH4
Kilometers
0
10
20
43.3˚S
43.4˚S
43.5˚S
43.6˚S
43.7˚S
43.8˚S
43.9˚S
171.6˚E
171.8˚E
172˚E
172.2˚E
172.4˚E
172.6˚E
172.8˚E
173˚E

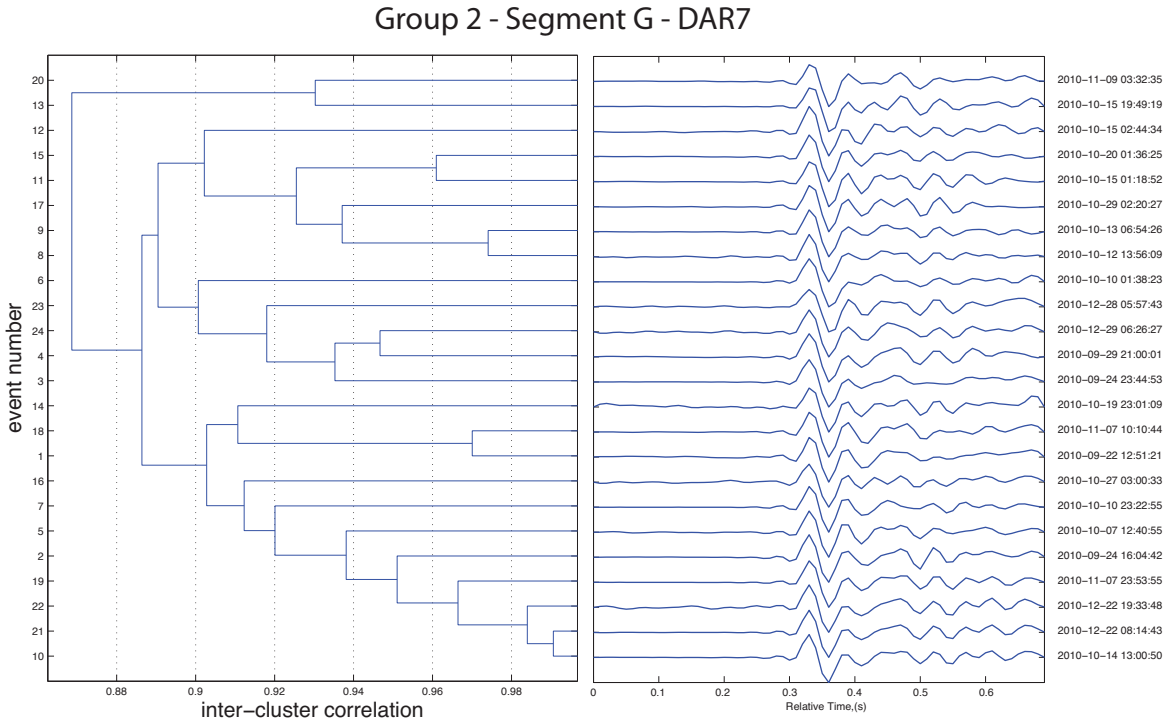
Group 2 - Segment G - DAR7
event number
inter−cluster correlation
Relative Time,(s)
2010−11−09 03:32:35
2010−10−15 19:49:19
2010−10−15 02:44:34
2010−10−20 01:36:25
2010−10−15 01:18:52
2010−10−29 02:20:27
2010−10−13 06:54:26
2010−10−12 13:56:09
2010−10−10 01:38:23
2010−12−28 05:57:43
2010−12−29 06:26:27
2010−09−29 21:00:01
2010−09−24 23:44:53
2010−10−19 23:01:09
2010−11−07 10:10:44
2010−09−22 12:51:21
2010−10−27 03:00:33
2010−10−10 23:22:55
2010−10−07 12:40:55
2010−09−24 16:04:42
2010−11−07 23:53:55
2010−12−22 19:33:48
2010−12−22 08:14:43
2010−10−14 13:00:50

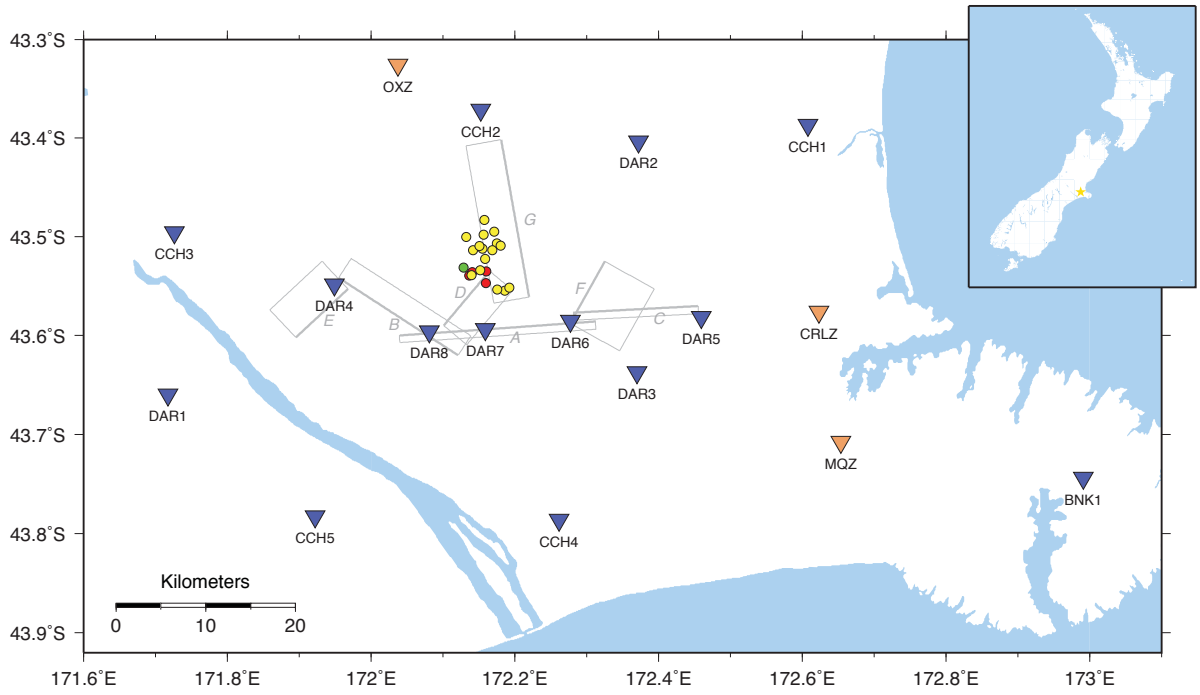
OXZ
CCH2
DAR2
CCH1
CCH3
DAR4
DAR8
DAR7
DAR6
DAR5
CRLZ
DAR3
DAR1
MQZ
BNK1
CCH5
CCH4
Kilometers
0
10
20
43.3˚S
43.4˚S
43.5˚S
43.6˚S
43.7˚S
43.8˚S
43.9˚S
171.6˚E
171.8˚E
172˚E
172.2˚E
172.4˚E
172.6˚E
172.8˚E
173˚E

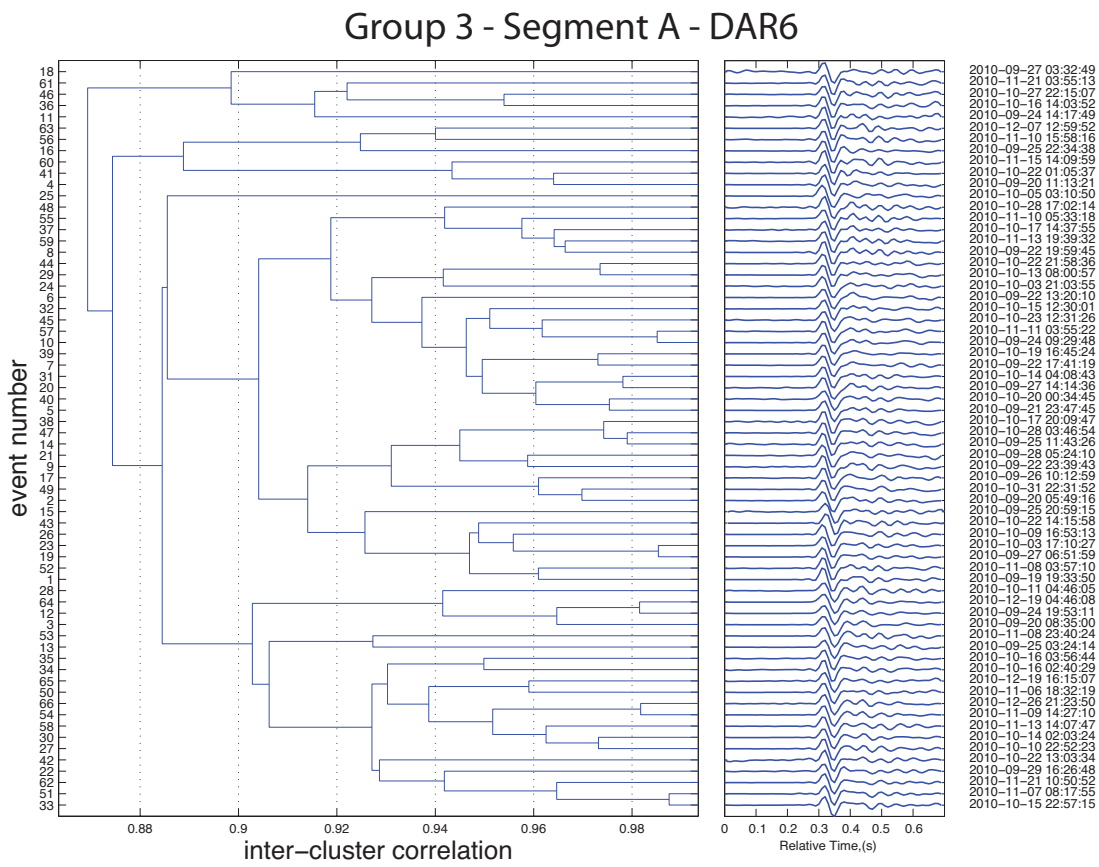
Group 3 - Segment A - DAR6
event number
inter−cluster correlation
0.88
0.9
0.92
0.94
0.96
0.98
0
0.1
0.2
0.3
0.4
0.5
0.6
Relative Time,(s)
2010−09−27 03:32:49
2010−11−21 03:55:13
2010−10−27 22:15:07
2010−10−16 14:03:52
2010−09−24 14:17:49
2010−12−07 12:59:52
2010−11−10 15:58:16
2010−09−25 22:34:38
2010−11−15 14:09:59
2010−10−22 01:05:37
2010−09−20 11:13:21
2010−10−05 03:10:50
2010−10−28 17:02:14
2010−11−10 05:33:18
2010−10−17 14:37:55
2010−11−13 19:39:32
2010−09−22 19:59:45
2010−10−22 21:58:36
2010−10−13 08:00:57
2010−10−03 21:03:55
2010−09−22 13:20:10
2010−10−15 12:30:01
2010−10−23 12:31:26
2010−11−11 03:55:22
2010−09−24 09:29:48
2010−10−19 16:45:24
2010−09−22 17:41:19
2010−10−14 04:08:43
2010−09−27 14:14:36
2010−10−20 00:34:45
2010−09−21 23:47:45
2010−10−17 20:09:47
2010−10−28 03:46:54
2010−09−25 11:43:26
2010−09−28 05:24:10
2010−09−22 23:39:43
2010−09−26 10:12:59
2010−10−31 22:31:52
2010−09−20 05:49:16
2010−09−25 20:59:15
2010−10−22 14:15:58
2010−10−09 16:53:13
2010−10−03 17:10:27
2010−09−27 06:51:59
2010−11−08 03:57:10
2010−09−19 19:33:50
2010−10−11 04:46:05
2010−12−19 04:46:08
2010−09−24 19:53:11
2010−09−20 08:35:00
2010−11−08 23:40:24
2010−09−25 03:24:14
2010−10−16 03:56:44
2010−10−16 02:40:29
2010−12−19 16:15:07
2010−11−06 18:32:19
2010−12−26 21:23:50
2010−11−09 14:27:10
2010−11−13 14:07:47
2010−10−14 02:03:24
2010−10−10 22:52:23
2010−10−22 13:03:34
2010−09−29 16:26:48
2010−11−21 10:50:52
2010−11−07 08:17:55
2010−10−15 22:57:15

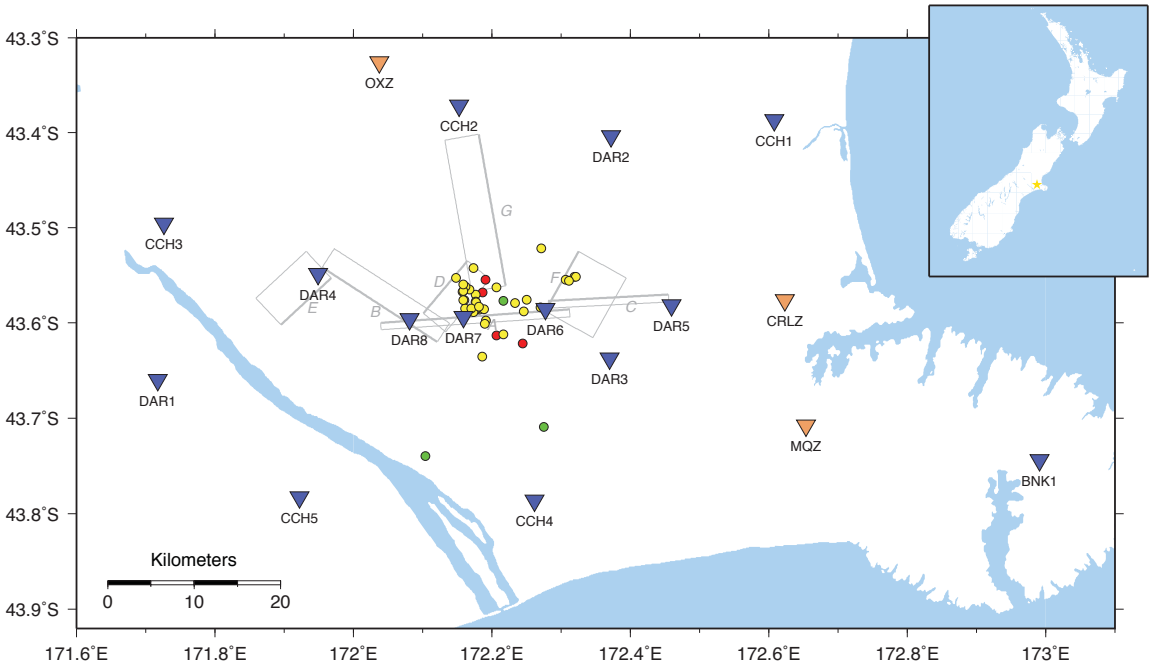
43.3˚S
43.4˚S
43.5˚S
43.6˚S
43.7˚S
43.8˚S
43.9˚S
171.6˚E
171.8˚E
172˚E
172.2˚E
172.4˚E
172.6˚E
172.8˚E
173˚E
OXZ
CCH2
DAR2
CCH1
CCH3
DAR4
DAR8
DAR7
DAR6
DAR5
DAR3
DAR1
CRLZ
MQZ
BNK1
CCH5
CCH4
G
D
F
E
B
A
C
Kilometers
0
10
20

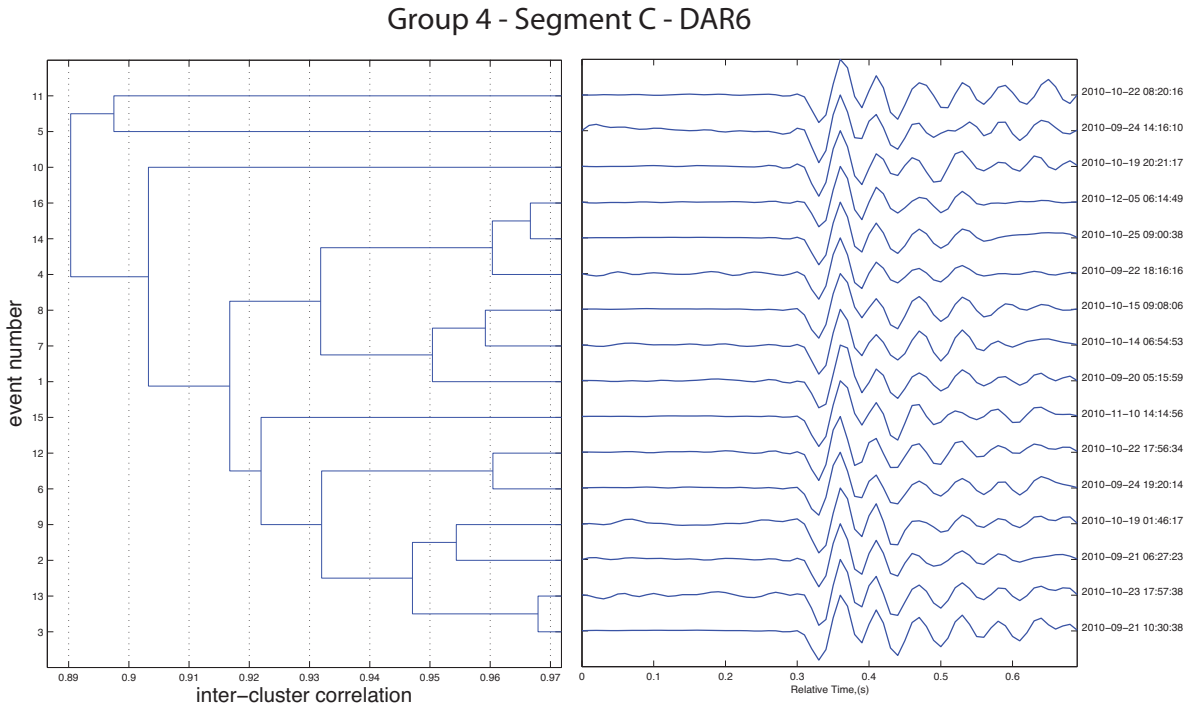
Group 4 - Segment C - DAR6
event number
inter–cluster correlation
Relative Time,(s)
2010–10–22 08:20:16
2010–09–24 14:16:10
2010–10–19 20:21:17
2010–12–05 06:14:49
2010–10–25 09:00:38
2010–09–22 18:16:16
2010–10–15 09:08:06
2010–10–14 06:54:53
2010–09–20 05:15:59
2010–11–10 14:14:56
2010–10–22 17:56:34
2010–09–24 19:20:14
2010–10–19 01:46:17
2010–09–21 06:27:23
2010–10–23 17:57:38
2010–09–21 10:30:38

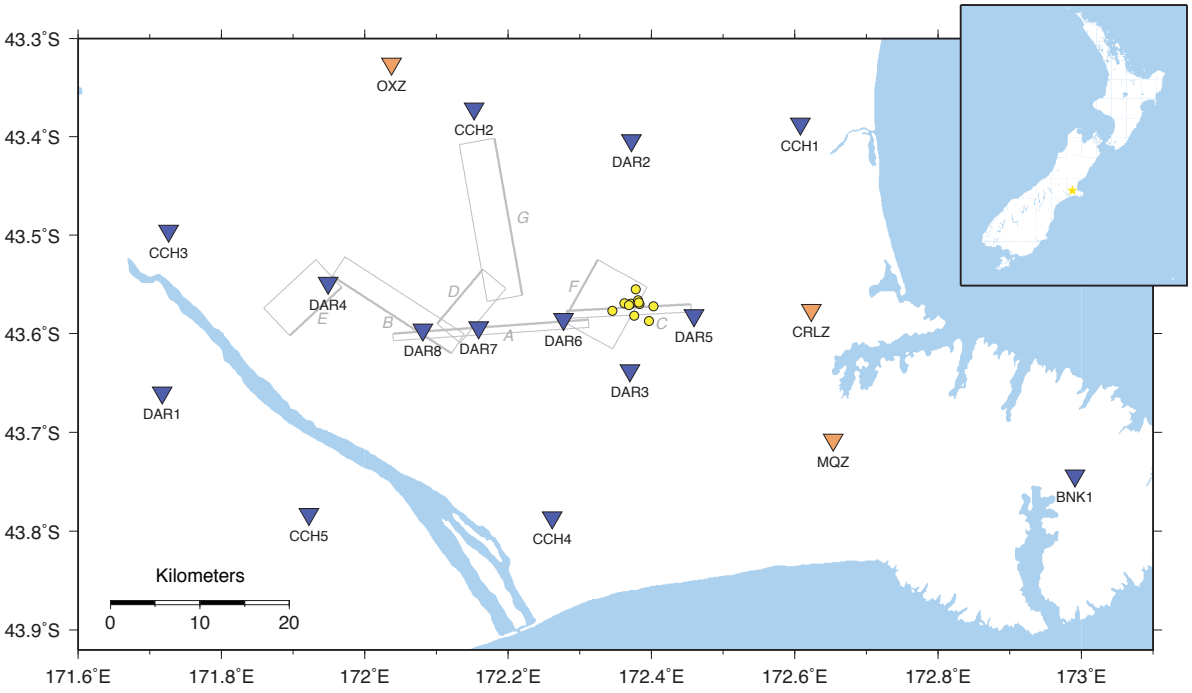
OXZ
CCH2
DAR2
CCH1
CCH3
DAR4
DAR8
DAR7
DAR6
DAR5
DAR3
CRLZ
DAR1
MQZ
BNK1
CCH5
CCH4
Kilometers
0
10
20
43.3˚S
43.4˚S
43.5˚S
43.6˚S
43.7˚S
43.8˚S
43.9˚S
171.6˚E
171.8˚E
172˚E
172.2˚E
172.4˚E
172.6˚E
172.8˚E
173˚E

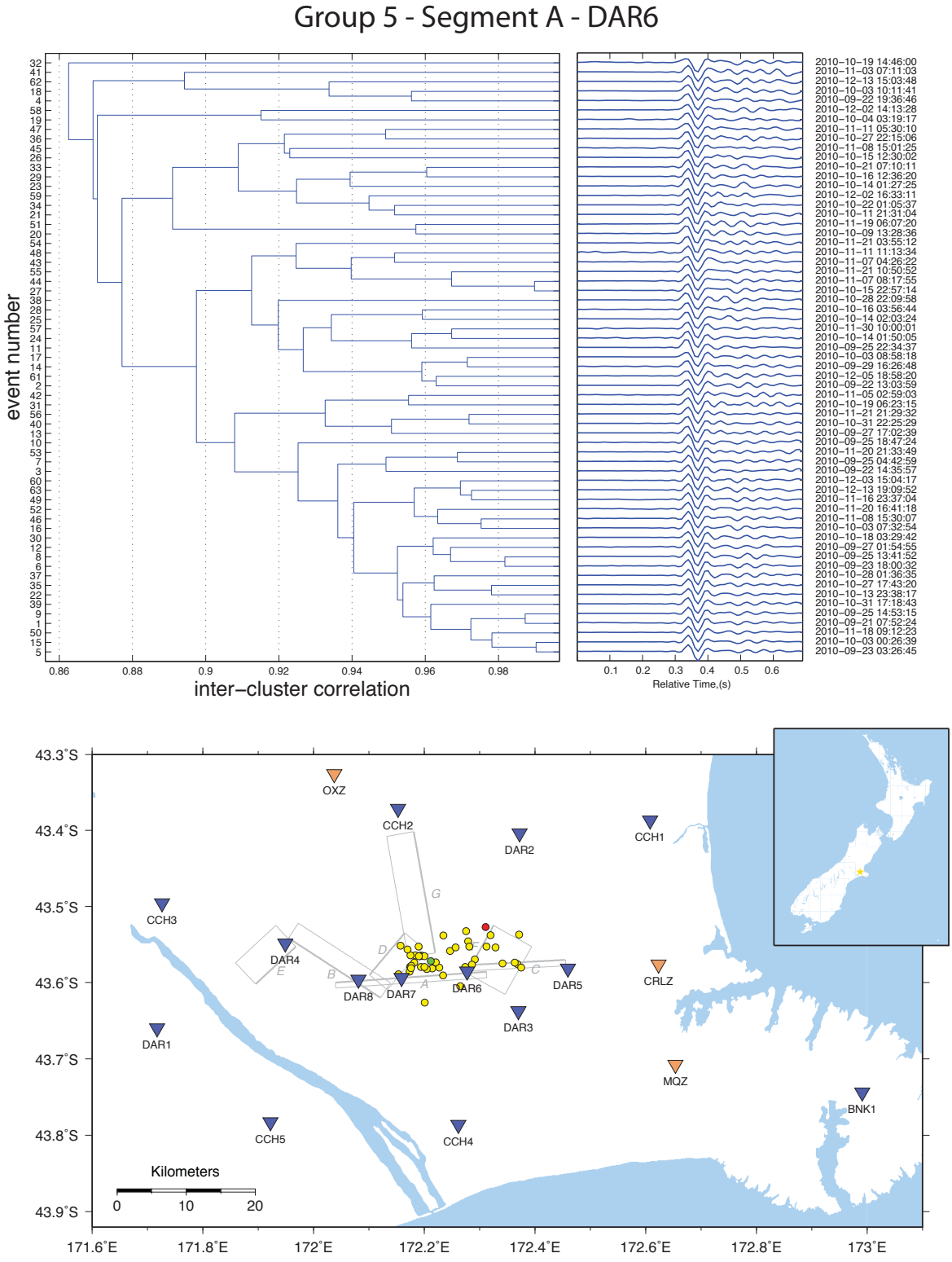
Group 5 - Segment A - DAR6
event number
inter−cluster correlation
0.86
0.88
0.9
0.92
0.94
0.96
0.98
Relative Time,(s)
0.1
0.2
0.3
0.4
0.5
0.6
2010−10−19 14:46:00
2010−11−03 07:11:03
2010−12−13 15:03:48
2010−10−03 10:11:41
2010−09−22 19:36:46
2010−12−02 14:13:28
2010−10−04 03:19:17
2010−11−11 05:30:10
2010−10−27 22:15:06
2010−11−08 15:01:25
2010−10−15 12:30:02
2010−10−21 07:10:11
2010−10−16 12:36:20
2010−10−14 01:27:25
2010−12−02 16:33:11
2010−10−22 01:05:37
2010−10−11 21:31:04
2010−11−19 06:07:20
2010−10−09 13:28:36
2010−11−21 03:55:12
2010−11−11 11:13:34
2010−11−07 04:26:22
2010−11−21 10:50:52
2010−11−07 08:17:55
2010−10−15 22:57:14
2010−10−28 22:09:58
2010−10−16 03:56:44
2010−10−14 02:03:24
2010−11−30 10:00:01
2010−10−14 01:50:05
2010−09−25 22:34:37
2010−10−03 08:58:18
2010−09−29 16:26:48
2010−12−05 18:58:20
2010−09−22 13:03:59
2010−11−05 02:59:03
2010−10−19 06:23:15
2010−11−21 21:29:32
2010−10−31 22:25:29
2010−09−27 17:02:39
2010−09−25 18:47:24
2010−11−20 21:33:49
2010−09−25 04:42:59
2010−09−22 14:35:57
2010−12−03 15:04:17
2010−12−13 19:09:52
2010−11−16 23:37:04
2010−11−20 16:41:18
2010−11−08 15:30:07
2010−10−03 07:32:54
2010−10−18 03:29:42
2010−09−27 01:54:55
2010−09−25 13:41:52
2010−09−23 18:00:32
2010−10−28 01:36:35
2010−10−27 17:43:20
2010−10−13 23:38:17
2010−10−31 17:18:43
2010−09−25 14:53:15
2010−09−21 07:52:24
2010−11−18 09:12:23
2010−10−03 00:26:39
2010−09−23 03:26:45
43.3°S
43.4°S
43.5°S
43.6°S
43.7°S
43.8°S
43.9°S
171.6°E
171.8°E
172°E
172.2°E
172.4°E
172.6°E
172.8°E
173°E
OXZ
CCH2
DAR2
CCH1
CCH3
DAR4
DAR8
DAR7
DAR6
DAR5
CRLZ
DAR3
DAR1
MQZ
BNK1
CCH5
CCH4
A
B
C
D
E
F
G
Kilometers
0
10
20

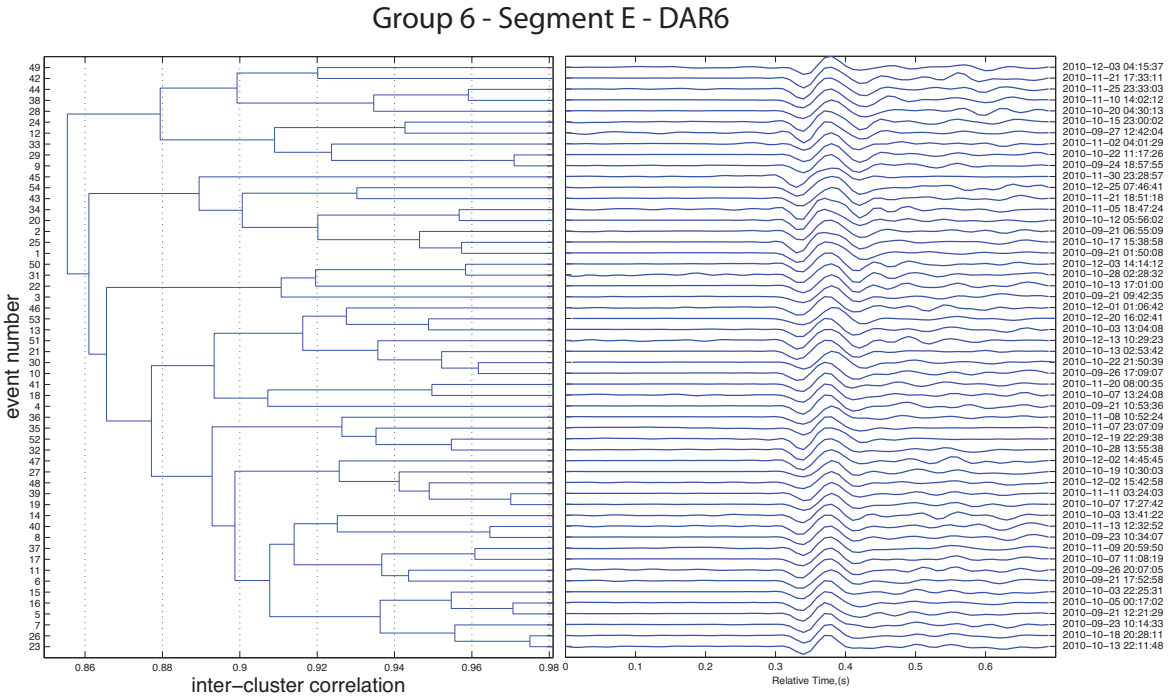
Group 6 - Segment E - DAR6
event number
inter−cluster correlation
0.86
0.88
0.9
0.92
0.94
0.96
0.98
Relative Time,(s)
0
0.1
0.2
0.3
0.4
0.5
0.6

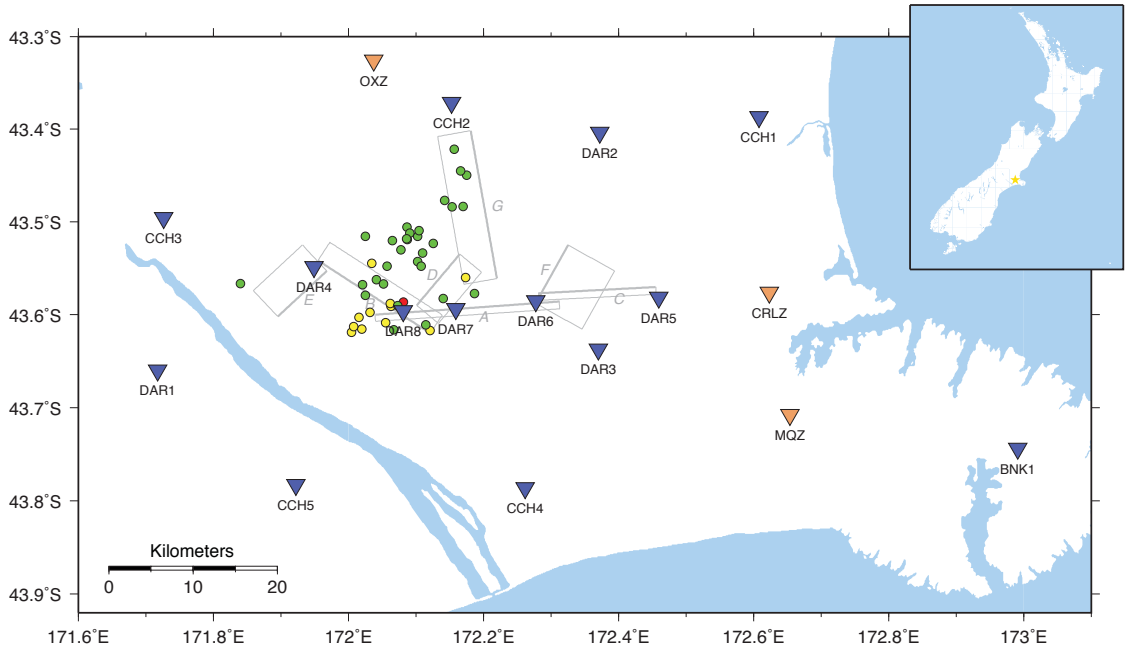
43.3°S
43.4°S
43.5°S
43.6°S
43.7°S
43.8°S
43.9°S
171.6°E
171.8°E
172°E
172.2°E
172.4°E
172.6°E
172.8°E
173°E
OXZ
CCH2
DAR2
CCH1
CCH3
DAR4
DAR8
DAR7
DAR6
DAR5
DAR3
CRLZ
DAR1
MQZ
BNK1
CCH5
CCH4
Kilometers
0
10
20
A
B
C
D
E
F
G

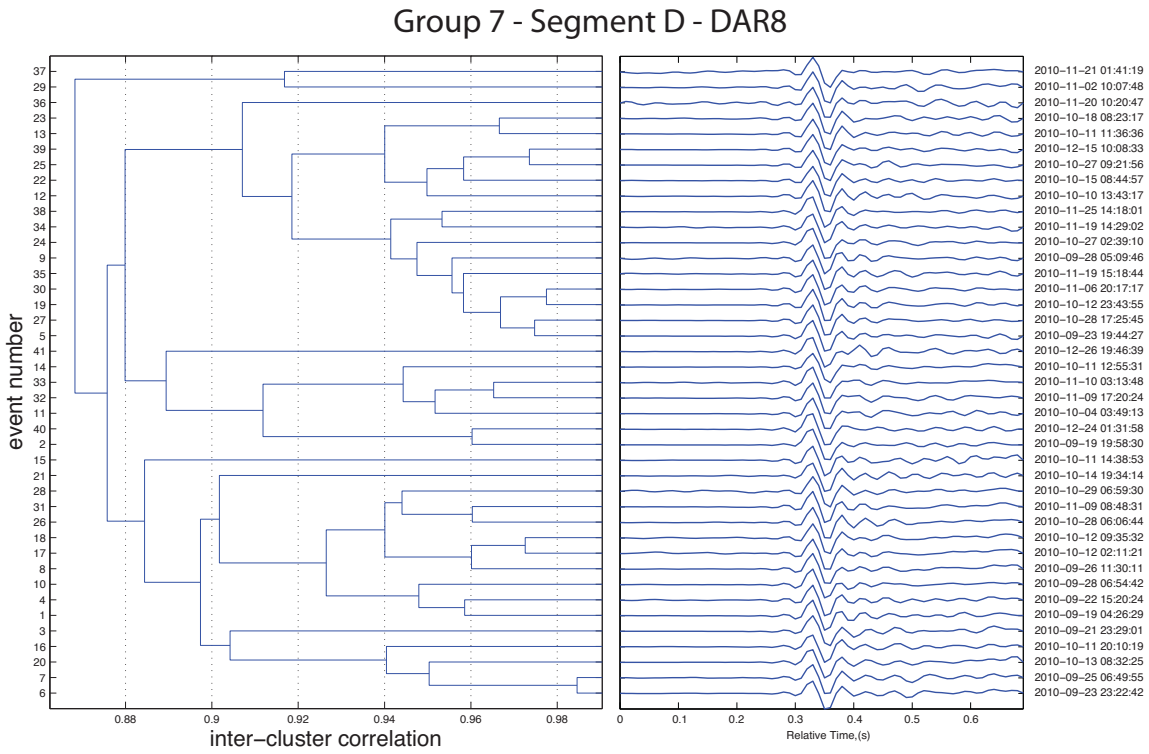
Group 7 - Segment D - DAR8
event number
inter–cluster correlation
Relative Time,(s)
2010–11–21 01:41:19
2010–11–02 10:07:48
2010–11–20 10:20:47
2010–10–18 08:23:17
2010–10–11 11:36:36
2010–12–15 10:08:33
2010–10–27 09:21:56
2010–10–15 08:44:57
2010–10–10 13:43:17
2010–11–25 14:18:01
2010–11–19 14:29:02
2010–10–27 02:39:10
2010–09–28 05:09:46
2010–11–19 15:18:44
2010–11–06 20:17:17
2010–10–12 23:43:55
2010–10–28 17:25:45
2010–09–23 19:44:27
2010–12–26 19:46:39
2010–10–11 12:55:31
2010–11–10 03:13:48
2010–11–09 17:20:24
2010–10–04 03:49:13
2010–12–24 01:31:58
2010–09–19 19:58:30
2010–10–11 14:38:53
2010–10–14 19:34:14
2010–10–29 06:59:30
2010–11–09 08:48:31
2010–10–28 06:06:44
2010–10–12 09:35:32
2010–10–12 02:11:21
2010–09–26 11:30:11
2010–09–28 06:54:42
2010–09–22 15:20:24
2010–09–19 04:26:29
2010–09–21 23:29:01
2010–10–11 20:10:19
2010–10–13 08:32:25
2010–09–25 06:49:55
2010–09–23 23:22:42

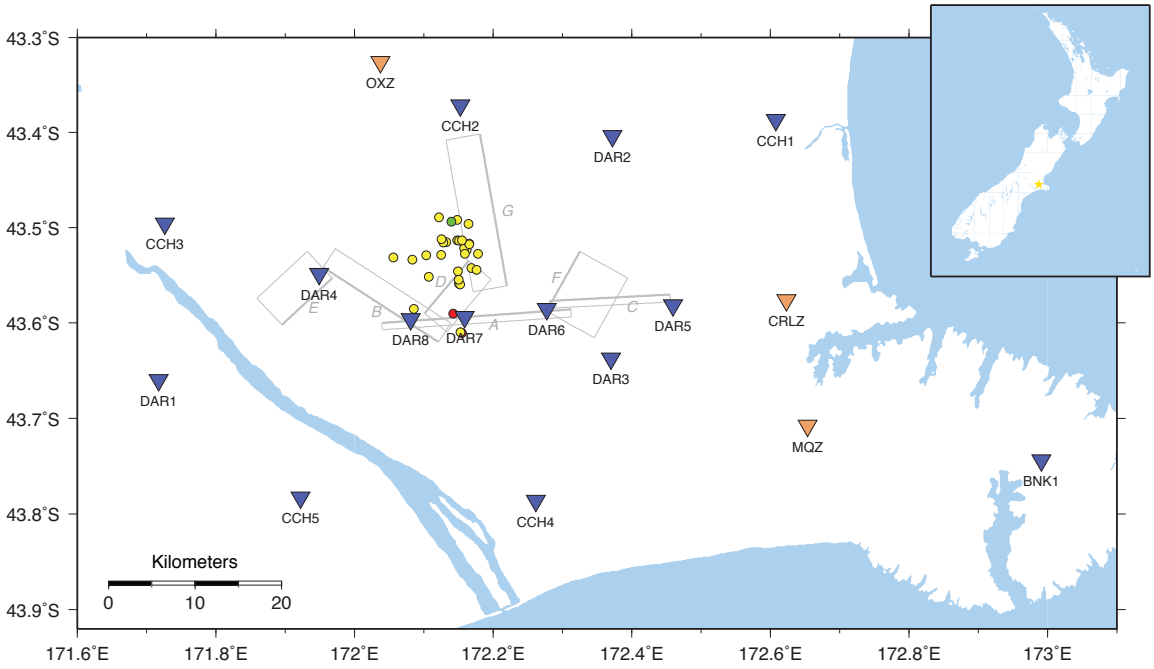
OXZ
CCH2
DAR2
CCH1
CCH3
DAR4
DAR8
DAR7
DAR6
DAR5
CRLZ
DAR3
DAR1
MQZ
BNK1
CCH5
CCH4
Kilometers
0
10
20
43.3˚S
43.4˚S
43.5˚S
43.6˚S
43.7˚S
43.8˚S
43.9˚S
171.6˚E
171.8˚E
172˚E
172.2˚E
172.4˚E
172.6˚E
172.8˚E
173˚E

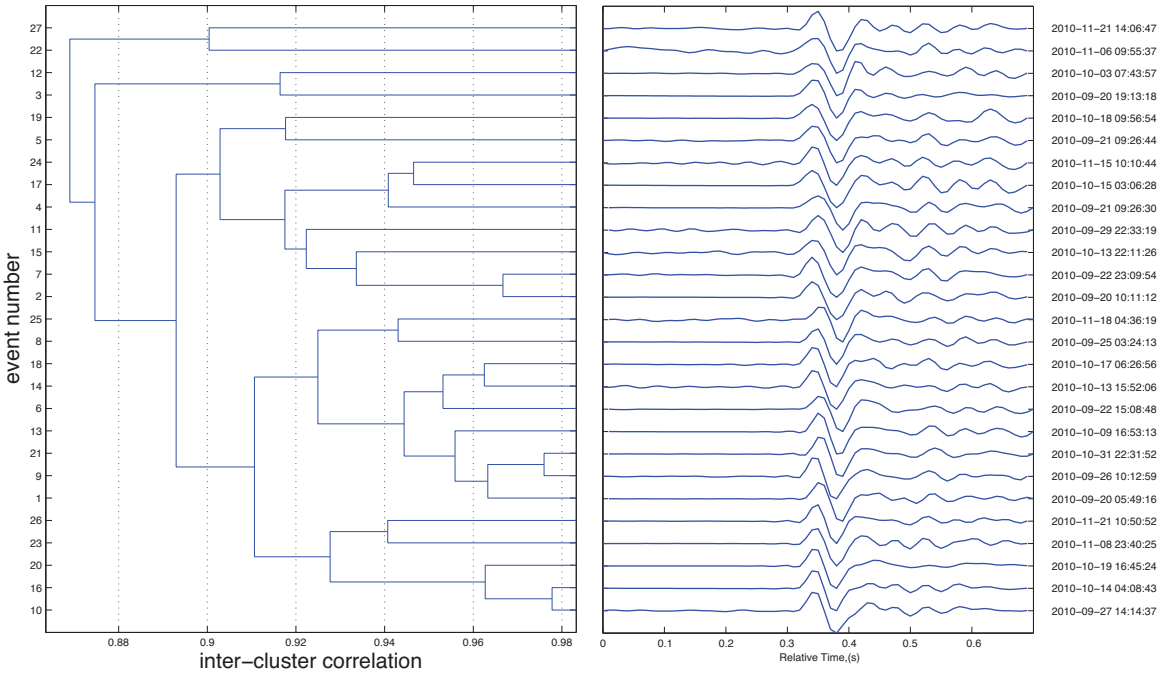
Group 8 - Segment C - DAR6
event number
inter–cluster correlation
Relative Time,(s)
2010–11–21 14:06:47
2010–11–06 09:55:37
2010–10–03 07:43:57
2010–09–20 19:13:18
2010–10–18 09:56:54
2010–09–21 09:26:44
2010–11–15 10:10:44
2010–10–15 03:06:28
2010–09–21 09:26:30
2010–09–29 22:33:19
2010–10–13 22:11:26
2010–09–22 23:09:54
2010–09–20 10:11:12
2010–11–18 04:36:19
2010–09–25 03:24:13
2010–10–17 06:26:56
2010–10–13 15:52:06
2010–09–22 15:08:48
2010–10–09 16:53:13
2010–10–31 22:31:52
2010–09–26 10:12:59
2010–09–20 05:49:16
2010–11–21 10:50:52
2010–11–08 23:40:25
2010–10–19 16:45:24
2010–10–14 04:08:43
2010–09–27 14:14:37

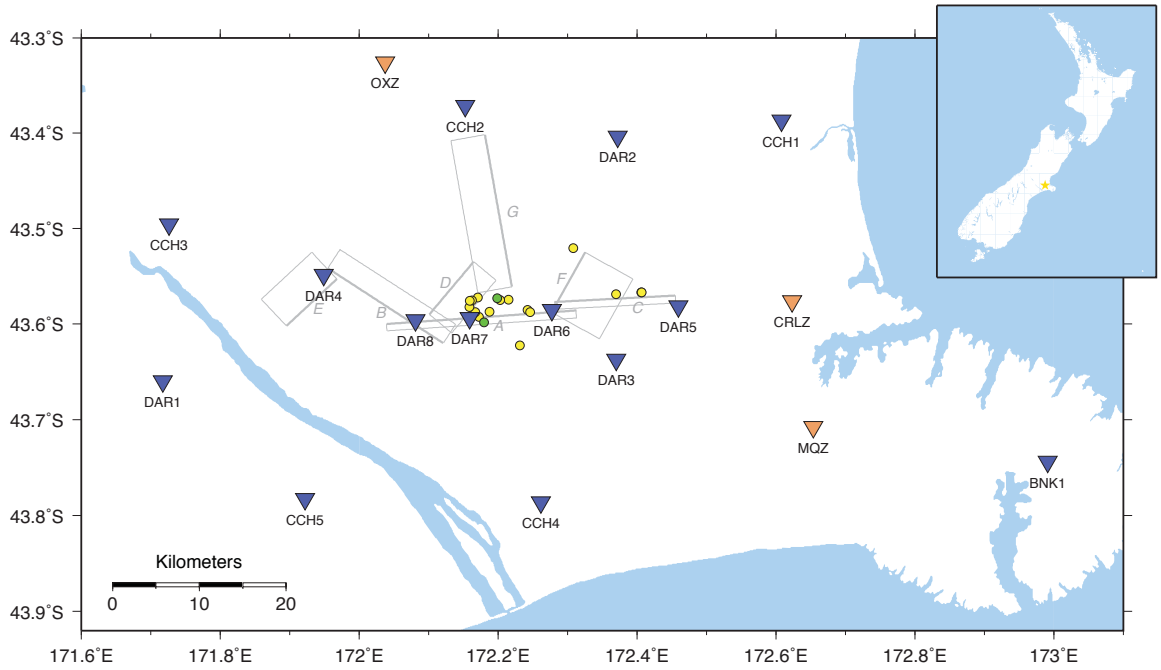
OXZ
CCH2
DAR2
CCH1
CCH3
DAR4
DAR8
DAR7
DAR6
DAR5
DAR3
CRLZ
DAR1
MQZ
BNK1
CCH5
CCH4
Kilometers
43.3˚S
43.4˚S
43.5˚S
43.6˚S
43.7˚S
43.8˚S
43.9˚S
171.6˚E
171.8˚E
172˚E
172.2˚E
172.4˚E
172.6˚E
172.8˚E
173˚E